GEOPHYSICS, VOL. 81, NO. 3 (MAY-JUNE 2016); P. D263–D281, 24 FIGS., 6 TABLES.
10.1190/GEO2015-0514.1

On the evolution of the elastic properties of organic-rich shale upon pyrolysis-induced thermal maturation

Adam M. Allan[1], Anthony C. Clark[1], Tiziana Vanorio[1], Waruntorn Kanitpanyacharoen[2], and Hans-Rudolf Wenk[3]

ABSTRACT

The evolution of the elastic properties of organic-rich shale as a function of thermal maturity remains poorly constrained. This understanding is pivotal to the characterization of source rocks and unconventional reservoirs. To better constrain the evolution of the elastic properties and microstructure of organic-rich shale, we have studied the acoustic velocities and elastic anisotropy of samples from two microstructurally different organic-rich shales before and after pyrolysis-induced thermal maturation. To more physically imitate in situ thermal maturation, we performed the pyrolysis experiments on intact core plugs under applied reservoir-magnitude confining pressures. Iterative characterization of the elastic properties of a clay-rich, laminar Barnett Shale sample documents the development of subparallel to bedding cracks by an increase in velocity sensitivity to pressure perpendicular to the bedding. These cracks, however, are not visible through time-lapse scanning electron microscope imaging, indicating either submicrometer crack apertures or predominant development within the core of the sample. At elevated confining pressures, in the absence of pore pressure, these induced cracks close, at which point, the sample is acoustically indistinguishable from the prepyrolysis sample. Conversely, a micritic Green River sample does not exhibit the formation of aligned compliant features. Rather, the sample exhibits a largely directionally independent decrease in velocity as load-bearing, pore-filling kerogen is removed from the sample. Due to the weak alignment of minerals, there is comparatively little intrinsic anisotropy; further, due to the relatively directionally independent evolution of velocity, the evolution of the anisotropy as a function of thermal maturity is not indicative of aligned compliant features. Our results have indicated that horizons of greater thermal maturity may be acoustically detectable in situ through increases in the elastic anisotropy of laminar shales or decreases in the acoustic velocities of nonlaminar shales, micritic rocks, or siltstones.

INTRODUCTION

The investigation of the interplay of organic geochemistry, shale microstructure, and rock-physical properties is a first step toward improving the characterization of source rocks and unconventional reservoirs. By understanding the relationship between the thermal maturity of the organic matter (i.e., the degree of hydrocarbon generation) and the elastic properties of the composite organic-rich shale, we may provide important inputs to rock-physical models that better improve the characterization and development of unconventional reservoirs. For instance, the effect of velocity anisotropy on the determination of microseismic locations and mechanisms during hydraulic fracturing has been well documented lately (e.g., Grechka et al., 2011; Li et al., 2014). By establishing deeper understanding of the elastic evolution of organic-rich shale as it thermally matures, experimental rock physicists may provide inputs and parameters that improve the processing and analysis of microseismic studies. Further, the quantification of the elastic tensor and elastic anisotropy of shale from well logs has received recent attention (e.g., Chesnokov et al., 2010; Sayers et al., 2015). The ability to relate

Manuscript received by the Editor 28 September 2015; revised manuscript received 24 January 2016; published online 20 April 2016.
[1]Stanford University, Stanford Rock Physics Laboratory, Stanford, California, USA. E-mail: adamm.allan@gmail.com; clarkac@stanford.edu; tvanorio@stanford.edu.
[2]Stanford University, Stanford Rock Physics Laboratory, Stanford, California, USA and Chulalongkorn University, Department of Geology, Faculty of Science, Bangkok, Thailand. E-mail: janekanit85@gmail.com; waruntorn.k@chula.ac.th.
[3]University of California Berkeley, Department of Earth and Planetary Science, Berkeley, California, USA. E-mail: wenk@berkeley.edu.

well-derived anisotropy measurements to thermal maturity through laboratory-derived relationships may, in combination with organic richness estimates (e.g., Passey et al., 1990), provide more robust estimates of horizon quality from well logs.

The generation of fluid hydrocarbons from solid organic matter in the tight pore space of shale increases the fluid pressure within isolated pores in and around organic bodies. The relaxation of this accumulated pore pressure is dependent upon the migration of generated hydrocarbons along pressure-induced, micron-scale cracks (microcracks) propagating through the mineral matrix of the rock. When open, and sufficiently coaligned, these microcracks may alter the elastic anisotropy of the shale. The slow deposition from suspension and burial-induced compaction of clay platelets typically generates a strongly anisotropic rock frame in shales, which is preserved in the absence of bioturbation (Kaarsberg, 1959; Jones and Wang, 1981; Vernik and Nur, 1992; Johnston and Christensen, 1995; Hornby, 1998; Wang, 2002; Vasin et al., 2013; Allan et al., 2015), although induced, coaligned microcracks can significantly alter this intrinsic anisotropy (Vernik, 1993; Johnston and Christensen, 1995; Dewhurst and Siggins, 2006; Allan et al., 2014). The magnitude of the crack-induced alteration of elastic anisotropy will depend on the number of cracks, the degree of alignment, and their aperture as a function of pressure, i.e., whether they are open or closed cracks. We hypothesize that there exists a thermal maturity dependence of the relevant crack parameters that will result in a thermal maturity dependence of the elastic anisotropy of organic-rich shale.

Previous attempts to identify thermal maturity-dependent trends in organic-rich shales have encountered a series of underlying issues. The primary contribution to the elastic evolution of shales with increasing thermal maturity is the so-called Vernik data set (Vernik and Nur, 1992; Vernik and Landis, 1996; Vernik and Liu, 1997). This data set documents a complex relationship between elastic anisotropy and thermal maturity (as represented by vitrinite reflectance; Figure 1). However, this data set draws on samples with widely varying mineralogies and depositional and burial histories. Subsequently, the interpretation of thermal maturity-dependent trends from this data set may be corrupted by the overprinting of mineralogical, depositional, or diagenetic effects (Figure 1).

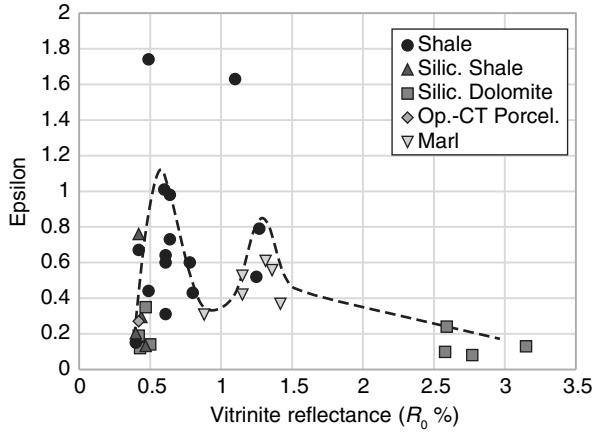

Figure 1. Unsaturated P-wave anisotropy, epsilon, at 5 MPa as a function of vitrinite reflectance, colored by reported lithology. Data are from Vernik and Nur (1992), Vernik and Landis (1996), and Vernik and Liu (1997), whereas the double peak trend line is adapted from Vanorio et al. (2008).

To remove the complicating factors arising from disparate sample provenances, we have initiated a program of iteratively characterizing individual organic-rich shale samples before and after inducing thermal maturation in the laboratory. Previous attempts at this methodology (Allan et al., 2014; Yenugu, 2014) induced thermal maturation through anhydrous pyrolysis experiments without applied effective pressure (the confining pressure minus the pore pressure). The combination of rapid hydrocarbon generation and lack of effective pressure resulted in the formation of aligned throughgoing fractures and microcracks with apertures on the order of tens of microns (Kobchenko et al., 2011; Allan et al., 2014; Yenugu, 2014). This fracturing of the rock and subsequent nonphysical increases of up to 1.25 in Thomsen's anisotropic parameter epsilon (Thomsen, 1986; Allan et al., 2014) must be minimized (or ideally removed entirely) to more robustly investigate the thermal maturity dependence of elastic anisotropy in organic-rich shale. Additionally, Zargari et al. (2011) conduct hydrous pyrolysis experiments on organic-rich Bakken samples; however, the retorting vessels used lacked any separation of the confining and pore spaces. As a result, the experiments were also conducted at zero-effective pressure. Further, Zargari et al. (2011) performed targeted nanoindentation measurements of the pyrolyzed organic matter, which prevents direct comparison of results with the acoustic measurements presented in this study.

In this study, we characterize the evolution of a pair of organic-rich mudstone samples before and after closed, anhydrous pyrolysis under applied confining pressure. The applied confining pressure serves to minimize fracturing and allows thermal maturation to occur under more physically representative conditions. This iterative characterization includes pre and postpyrolysis analysis of the microstructure, geochemistry, porosity, and acoustic velocity of Barnett Shale and Green River samples. In this manner, we provide a more complete characterization of the thermal evolution of each individual sample, while enabling a comparison of the respective evolutions of two different fine-grained, organic-rich rocks.

METHODS

In this section, we provide a mineralogical, microstructural, and geochemical description of the Barnett and Green River samples used in this study. This characterization is followed by a brief discussion of the rock-physics experiments conducted on each sample and a discussion of the purpose-built reactor designed to perform pyrolysis experiments under reservoir-magnitude confining pressures.

Sample characterization

The Mississippian Barnett Shale and Eocene Green River samples were provided precored by ENI S.p.A. and Chevron, respectively. The Barnett sample was provided predried, whereas the Green River sample was preserved in *n*-decane. Prior to all experiments, both samples were dried in an oven at 40°C until the mass loss stabilized to remove all free water with minimal alteration of the hydrated clay platelets. In this manner, there is no free water in the pore space of the dry sample, whereas there may remain considerable bound water in the clay and zeolite content. Each sample is composed of two plugs – one cored horizontally (or parallel to bedding) and one core vertically (or perpendicular to bedding; Figure 2).

Both samples were delivered as 2.5–5.0 cm long cylindrical plugs of approximately 2.5 cm diameter, and, due to the sample size requirements of different experimental techniques, they required subsampling.

To account for the destructive nature of geochemical characterization and the different sample sizes required for each experimental method, the horizontal and vertical plugs are subsampled as documented in Figure 2. The subsampling procedure results in approximately 2 cm long plugs for velocity analysis (vertical and horizontal) and an approximately 0.2 cm long horizontal coin for X-ray diffraction (XRD)-based microstructural and mineralogical characterization. The excess sample material and any irregularly shaped fragments are used for geochemical analysis. The geochemical analysis is performed by the Rock-Eval pyrolysis method at an external service laboratory.

Mineralogy and microstructure

To quantify the mineralogical composition and degree of crystallographic preferred orientation (CPO), high-energy synchrotron XRD experiments were conducted at beam-line 11-ID-C of the Advanced Photon Source (APS) at Argonne National Laboratory. The experimental procedure and details of data analysis with the Rietveld method follow the procedure described by Wenk et al. (2014). The diffraction images indicate a qualitatively significant preferred orientation by intensity variations of diffraction rings. The quantitative 3D orientation distributions (OD) and volume fractions of mineral species were refined (as in Wenk et al., 2014), and the OD's pole figures were calculated to display (001) pole densities projected on the bedding plane (Figure 3). The mineralogy and CPO of the two samples are documented in Tables 1 and 2.

As is clear from Table 1, the two samples have very different mineralogical compositions. The Barnett sample is a "classic" siliciclastic shale (91.7% clay and quartz) with auxiliary apatite (3.9%), pyrite (2.0%), and siderite (2.4%). Contrastingly, the Green River sample is predominantly composed of carbonates (17.9% calcite and 40.6% dolomite) with approximately equal parts of quartz (12.5%), analcime (13.8%), albite (11.6%), and very little clay (3.6%). The different mineralogies and geologic histories have an evident effect on the degree of crystallographic alignment exhibited by each sample as represented by the maximum value of the poles to the basal crystallographic planes (denoted by the Miller indices [001]; Table 2). The illite-mica and chlorite of the Barnett sample exhibit a strong alignment of (001) poles perpendicular to the bedding plane (Figure 3), over six times that for a sample with a random OD (noted as multiples of a random distribution; m.r.d.). Contrastingly, the Green River sample exhibits 40% less clay content by volume and a factor of two reduction in the alignment of clay minerals (Figure 3). In both samples, a significant portion of the clay minerals are randomly oriented as indicated by CPO minima of 0.2 and 0.7 m.r.d., respectively. Again, the Green River sample shows the greater degree of misalignment (Table 2). To remove the effect of the widely variable clay content of the two samples, we compare the "average degree of alignment" in each sample as in Allan et al. (2015) and equation 1, where CPO is the set of maximum (001) poles for each mineral and χ is the set of corresponding volume fractions:

$$\mathrm{CPO}_{\mathrm{avg}} = [\mathrm{CPO}_{\mathrm{max}}] \cdot [\chi]. \quad (1)$$

In this volume averaging process, all nonexplicitly aligned mineral phases are assumed to be randomly oriented, i.e., $[\mathrm{CPO}_{\mathrm{max}}] = 1$. As a result, we see that the average degree of crystallographic alignment is nearly 3.5 times greater in the Barnett sample than in the effectively randomly oriented, $\mathrm{CPO}_{\mathrm{max}} \sim 1$, Green River sample (Table 2).

The effect of composition on sample texture can also be seen through backscattered electron scanning electron microscope (BSE-SEM) imaging (Figure 4). The clay-rich Barnett Shale exhibits a strong alignment of the microcrystalline siliciclastic matrix and dispersed lenticular kerogen (OM). Additionally, there is some

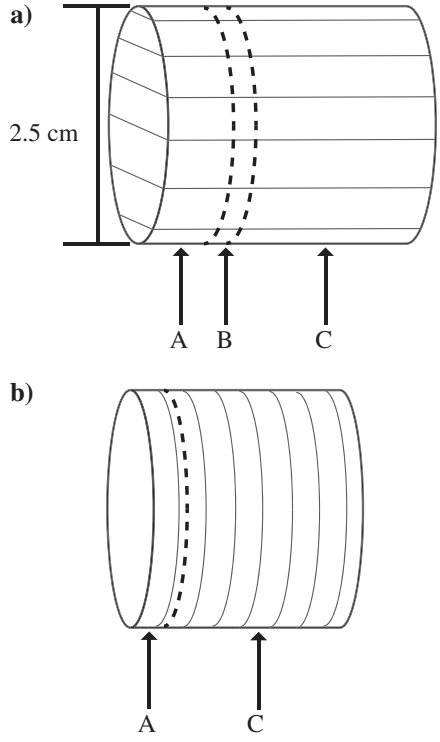

Figure 2. A schematic representation of the subsampling of the (a) horizontal and (b) vertical plugs. The labeled subsamples are: (A) excess material used for geochemical analysis, (B) a 0.2 cm thick coin for XRD experiments, and (C) an approximately 2.0 cm long plug for acoustic experiments.

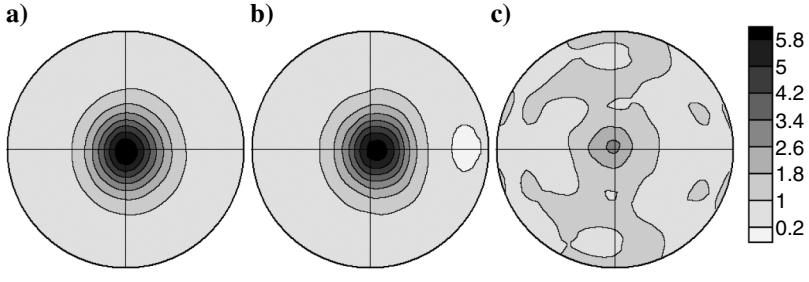

Figure 3. Basal (001) plane pole figures of (a) Barnett illite, (b) Barnett chlorite, and (c) Green River illite projected on the bedding plane. Equal area projection and linear contour scale in m.r.d. (see Table 2).

indication of stress- or deposition-induced alignment in the dispersed apatite grains. Contrastingly, the Green River samples exhibit a significantly lesser degree of alignment. Although lineations are visible in hand sample, these lineations correspond to mineralogical heterogeneities, i.e., organic-rich versus organic-lean lamina, rather than a pronounced mineralogical alignment. Indeed, the mineralogy and texture of the weakly aligned Green River sample are properly characterized as an argillaceous dolomicrite rather than as a shale. Additionally, the organic matter of the Green River does not occur as dispersed, coaligned lenses; rather, the kerogen occurs as a largely unstructured pore-filling phase.

The effective porosity of the samples is determined through helium porosimetry experiments. Given the mass and bulk volume of the sample (from caliper-derived length and diameter measurements, assuming a right circular cylindrical form), the effective porosity and grain density can be calculated from the helium porosimetry-derived grain volume measurements. The intrinsic experimental error is small (<0.05 cm^3); however, error in the bulk volume associated with irregularly shaped or chipped samples can result in errors in derived effective porosity values of up to a couple of porosity units. Because there may be a significant bound water or, postpyrolysis, produced hydrocarbons in the pore space, the effective porosity, as defined in this work, deviates subtly from the classical effective porosity. In this study, the effective porosity is the conventional effective porosity (the connected porosity), but less the porosity saturated by the residual hydrocarbons, e.g., a measurement of the unsaturated effective porosity. Due to the pore-filling nature of the organic matter in the Green River sample, the effective porosity of the rock is less than 1.5% (Table 3). The strongly textured Barnett sample, however, has an effective porosity of between 12% and 13%.

Subsequently, the samples characterized in this study form two, near-endmember points of comparison. A clay-rich, strongly aligned, laminar shale with dispersed, coaligned lenticular organic bodies (the Barnett sample), and a clay-poor effectively randomly oriented dolomicrite with unstructured pore-filling organic matter (the Green River sample). It is important to note that the Green River sample studied in this work is from a poorly aligned horizon within the formation and is not representative of the entire formation.

Geochemistry

Both samples used in this study are cored from outcrops to ensure that they are thermally immature prepyrolysis. Indeed, in Table 4, the Rock-Eval pyrolysis method indicator of thermal maturity T_{MAX} indicates that both samples are thermally immature ($T_{MAX} < 435$°C; Peters and Cassa, 1994). Furthermore, the quantity of hydrocarbons that can be generated via thermal maturation (S_2) indicates that both samples have excellent petroleum generation potential ($S_2 >$ 20 mg/g; Peters and Cassa, 1994). The hydrocarbon potential, equal to the sum of the retained free hydrocarbons S_1 and S_2, is 1.3 times greater for the Green River sample despite the sample containing 2.53% less total organic carbon (TOC) by weight. This apparent contradiction results from the 1.6 times greater hydrogen index of the lacustrine type I organic matter in the Green River relative to the marine type II organic matter of the Barnett Shale. Each gram of type I TOC in the Green River sample contains 1.6 times more hydrocarbons than an equivalent gram of Barnett sample, type II, TOC.

Table 1. The mineralogy of the Barnett and Green River samples in volume percent. Abbreviated clay minerals are illite-mica (Ill-mca), illite-smectite (Ill-sm), chlorite (Chl), and kaolinite (Kln). In the Barnett sample analysis, illite-mica and illite-smectite were not separated. All values in this table are derived from the plug cored parallel to bedding.

Sample	Clays				Quartz	Calcite	Dolomite	Others
	Ill-mca	Ill-sm	Chl	Kln				
Barnett	46.6		2.6	1.1	41.4	–	–	8.3
Green River	3.6	–	–	–	12.5	17.9	40.6	25.4

Table 2. Mineral CPO data as acquired from XRD experiments. Basal (001) plane pole figure maxima and minima are given in units of m.r.d. (Kocks et al., 2000; see Figure 3). The sample average value is computed as in equation 1. Dashes indicate that the volume fraction of the phase is too small to be considered for texture analysis.

Sample	Clays		Sample Avg
	Illite	Chlorite	
Barnett	6.6/0.3	6.0/0.2	3.74
Green River	2.9/0.7	–	1.07

Pulse transmission acoustic experiments

Acoustic velocity experiments were performed, using the pulse transmission method, on both plug orientations. A −400 V square pulse was sent to transducers with resonant frequencies of approximately 1 MHz, housed in 1 in. diameter endcaps. By using two orthogonally cored plugs, our system enables the characterization of five acoustic phases — $V_P(0°)$, $V_P(90°)$, $V_S(0°)$, $V_{SV}(90°)$, and $V_{SH}(90°)$, where V_P is the P-wave velocity and V_S is the S-wave velocity. For clarity, the propagation and polarization directions of each phase are schematically documented in Figure 5. The combination of these acoustic phases and bulk density ρ_B, enables the calculation of the elastic moduli and Thomsen anisotropy parameters, epsilon and gamma, as defined in equations 2–7. The error in P- and S-wave velocity measurements is approximately 1% and 2%, respectively, and the subsequent error in the calculated anisotropy values is between 3% and 6%:

$$C_{11} = \rho_B (V_P(90°))^2, \tag{2}$$

$$C_{33} = \rho_B (V_P(0°))^2, \tag{3}$$

$$C_{44} = \rho_B (V_{SV}(90°))^2, \tag{4}$$

$$C_{66} = \rho_B (V_{SH}(90°))^2, \quad (5)$$

$$\varepsilon = \frac{C_{11} - C_{33}}{2C_{33}}, \quad (6)$$

$$\gamma = \frac{C_{66} - C_{44}}{2C_{44}}. \quad (7)$$

The acoustic velocity is measured as a function of hydrostatic confining pressure, where the confining pressure loading and unloading cycles are shown in Figure 6. The confining fluid is prevented from entering the sample by a rubber jacket that allows stress transfer to the sample. During experiments, the axial sample strain is computed from sample length changes continuously monitored (with a resolution of approximately 8 s) by three external linear potentiometers. The radial strain is not monitored, but is assumed to correspond to the axial strain of the orthogonally oriented plug as detailed in Allan et al. (2014). These measurements are conducted in an unsaturated, drained configuration.

In our methodology, upon changing the confining pressure, the sample is left for 30 min to accommodate viscoelastic deformation. Figure 7a and 7b illustrates representative axial strain versus time curves for pressure steps from 2 to 5 MPa and from 30 to 40 MPa. It is clear that approximately 90% of the cumulative axial strain is purely elastic, and that within 5 min, 95% of the total axial strain has been attained. Concurrently, we have noted that although the sample continues to deform for some time after the change in pressure (and will continue to deform beyond the 30 min period), the acoustic velocity values for a hydrostatically confined sample change very little. P-wave velocities increase by no more than 60 m/s ($\leq 2\%$) over the first 10 min of viscoelastic compaction; however, further compaction has no resolvable effect on the velocity of the sample (Figure 7c). Subsequently, we infer that allowing for viscoelastic compaction for 30 min results in sufficiently settled samples for high-fidelity hydrostatically pressured acoustic velocity measurements. Further, we assume that 30 min is sufficient for any induced pore pressure gradients in the permeable pore network to equilibrate.

Confined, closed, anhydrous pyrolysis

Novel confined pyrolysis system

The thermal maturation of organic matter is typically represented as a first-order reaction as a function of temperature and time (e.g., Pepper and Corvi, 1995). Given the extreme lengths of time required to thermally mature organic matter and produce hydrocarbons at in situ temperatures, it is necessary that laboratory methods of inducing thermal maturation be conducted at elevated temperatures, generally greater than 300°C. Pyrolysis, the anoxic thermochemical decomposition of organic material, is a common experimental method for imitating in situ thermal maturation. Given the need in this work to pyrolyze whole core plugs and the difficulty associated with properly saturating those plugs, we perform anhydrous pyrolysis. Note, however, that these experiments are not truly anhydrous as there can be significant water bound in organic-, zeolite-, and clay-rich shale that will be released into the pore space at high temperature. The presence of this water may be important to the oil-to-gas ratio of hydrocarbons generated during pyrolysis experiments (Lewan, 1994). To more physically mimic in situ thermal maturation, we retain the products within the pore space (and a small volume of pore lines around the sample) and apply reservoir-scale, external confining pressure to the sample during pyrolysis. In this manner, we perform confined, closed, and anhydrous pyrolysis. To our knowledge, this work con-

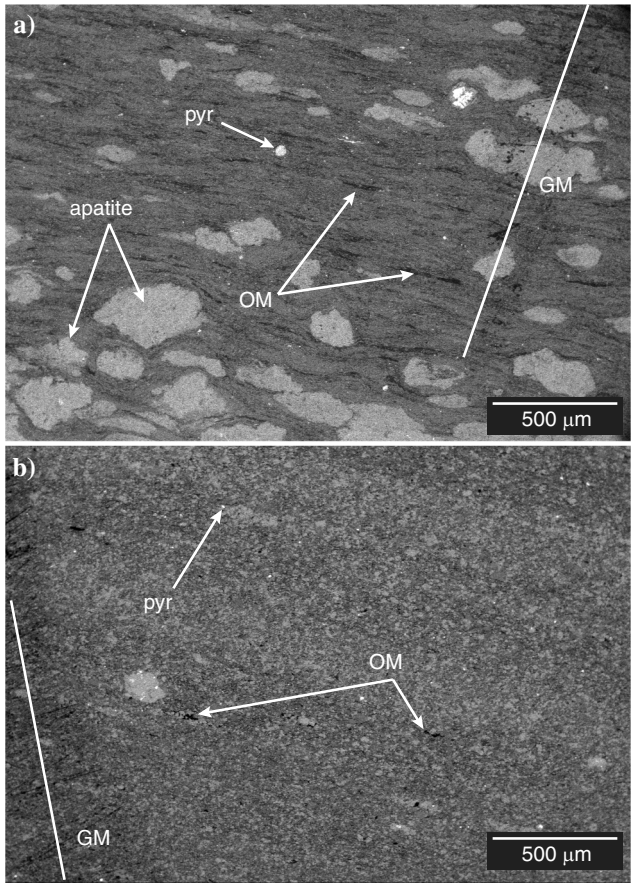

Figure 4. SEM images representative of the baseline, immature window microstructures of the horizontally cored (a) Barnett and (b) Green River samples. Identified features include organic matter (OM), pyrite (pyr), apatite, and graphite markings (GM) used to recover image locations postpyrolysis.

Table 3. The effective porosity and grain density of each subsample used in the velocity experiments.

Sample	Orientation	Effective porosity (%)	Grain density (g/cm^3)
Barnett	Horizontal	12.7 ± 0.5	2.30 ± 0.01
	Vertical	13.2 ± 0.4	2.32 ± 0.01
Green River	Horizontal	1.3 ± 0.3	2.29 ± 0.01
	Vertical	0.5 ± 0.5	2.26 ± 0.01

stitutes the first attempt at pyrolyzing whole core plugs under reservoir-magnitude applied confining pressure.

Confined, closed anhydrous pyrolysis experiments are conducted in our laboratory using a purpose-built, high-temperature/high-pressure (HTHP) reactor. The HTHP system is an internally heated pressure vessel with a maximum pressure rating of 34.5 MPa (5000 psi) at 510°C (950°F). The system consists of a 1 L volume, bolted closure reactor and is heated by a 200 W ceramic refractory heater. Due to the extreme temperatures used, in lieu of rubber tubing (melting point approximately 180°C), the sample is jacketed by annealed copper tubing to prevent the intrusion of confining fluid or the loss of generated hydrocarbons. The rock sample is thermally isolated by cylindrical alumina spacers. During experiments, the temperature is measured at a series of locations near the rock by a set of type-K thermocouples, one of which acts as the feedback sensor in a proportional-integral-derivative control loop. Further, thermocouples are used to monitor the temperature throughout the vessel and pore lines. The design of the HTHP is illustrated schematically in Figure 8.

Table 4. The geochemical properties of each sample as characterized by Rock-Eval analysis. Each pyrolysis experiment is represented by the programmed control temperature of the experiment (T_{CTRL}). The baseline, thermally immature values are included for convenient comparison and denoted by a T_{CTRL} of '-.' The geochemical properties reported include TOC, the free retained hydrocarbons (S_1), the thermally producible hydrocarbons (S_2), the Rock-Eval indicator of thermal maturity (T_{MAX}), and the hydrogen and oxygen indices (HI and OI, respectively). The parameters S_1 and S_2 are measured in milligrams of hydrocarbons per gram of dry rock.

Sample	T_{CTRL} (°C)	TOC (wt. %)	S_1 (mg/g)	S_2 (mg/g)	T_{MAX} (°C)	HI	OI
Barnett	–	11.67	2.32	55.98	418	480	9
	360	9.47	8.91	22.65	438	239	7
	425V	9.40	1.69	4.79	500	51	8
	425H	8.08	3.25	6.14	486	76	10
Green River	–	9.14	4.8	71.23	419	780	10
	380	6.43	19.25	39.72	427	617	10
	425V	4.10	12.34	6.92	439	170	17
	425H	3.14	3.25	2.08	480	66	22

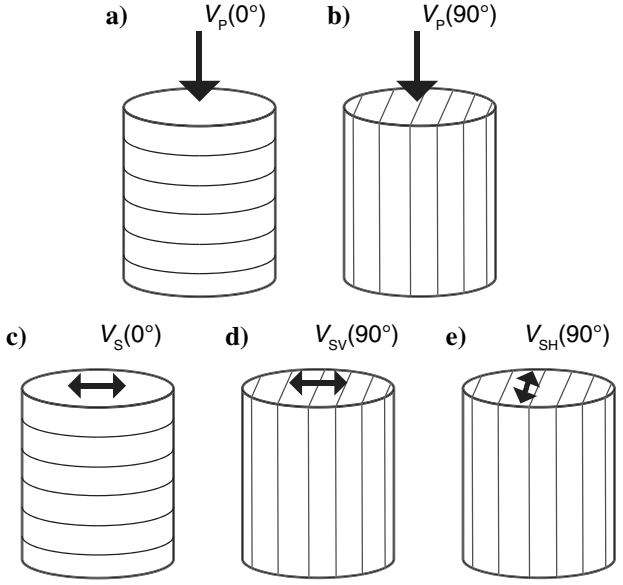

Figure 5. A schematic representation of the P- and S-wave phases recorded during acoustic velocity experiments after Allan et al. (2015). (a and c) Vertically propagating P- and S-waves, (b) horizontally propagating P-wave, and two horizontally propagating S-waves — (d) one polarized perpendicular to bedding and (e) the other polarized parallel to bedding.

Pyrolysis experimental protocol

Before each experiment, the pore space of the sample, sealed in the core holder, is vacuumed and flushed with argon gas to provide the anoxic environment required for kerogen pyrolysis. The confining space (which has also been vacuumed) is then filled to an initial pressure $P_1 \sim 10.6$ MPa, with argon at room temperature. The refractory heater then increases the temperature at the control sensor by 2°C/ min to a specified intermediate temperature — typically 300°C. This intermediate temperature is maintained for approximately 10 min. The temperature is then ramped to the final pyrolysis temperature at 0.5°C/ min. The system is held at this final temperature for 72 h. Due to thermal expansion of the confining argon, the confining pressure attains a greater value ($P_2 \sim 24$ MPa) upon heating. After 72 h, the temperature is ramped down at 2°C/ min to 100°C and then allowed to cool to room temperature over approximately 16 h.

The above protocol was followed for all experiments. Specifically, the oil window was reached by pyrolysis at 360°C and 380°C, for the Barnett and Green River samples, respectively, at 22–24 MPa for 72 h. For both samples, the gas window was reached by pyrolysis at 425°C at 22–24 MPa for 72 h. The geochemical validation of the pyrolysis procedure is documented in the "Results" section.

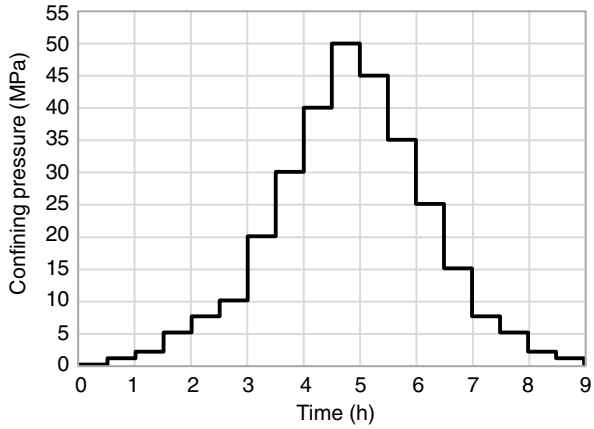

Figure 6. A schematic representation of the confining pressures at which waveform arrival times are measured as a function of experimental time.

The pressure and temperature behavior as a function of time during a typical gas window pyrolysis experiment for a Green River sample is shown in Figure 9. Thermal expansion of the argon in the pore space causes a clear increase in pore pressure during the heating phase — at this time, the liberation and evaporation of bound water, if present, will also increase the pore pressure. During the 72 h pyrolysis period, the pore pressure increases, with a decaying rate, as a function of time — this signal is attributed to the generation of hydrocarbons in the pore space. After cooling to room temperature, in this example, there is a 1.41 MPa increase in pore pressure attributable to generated reaction products, i.e., hydrocarbons.

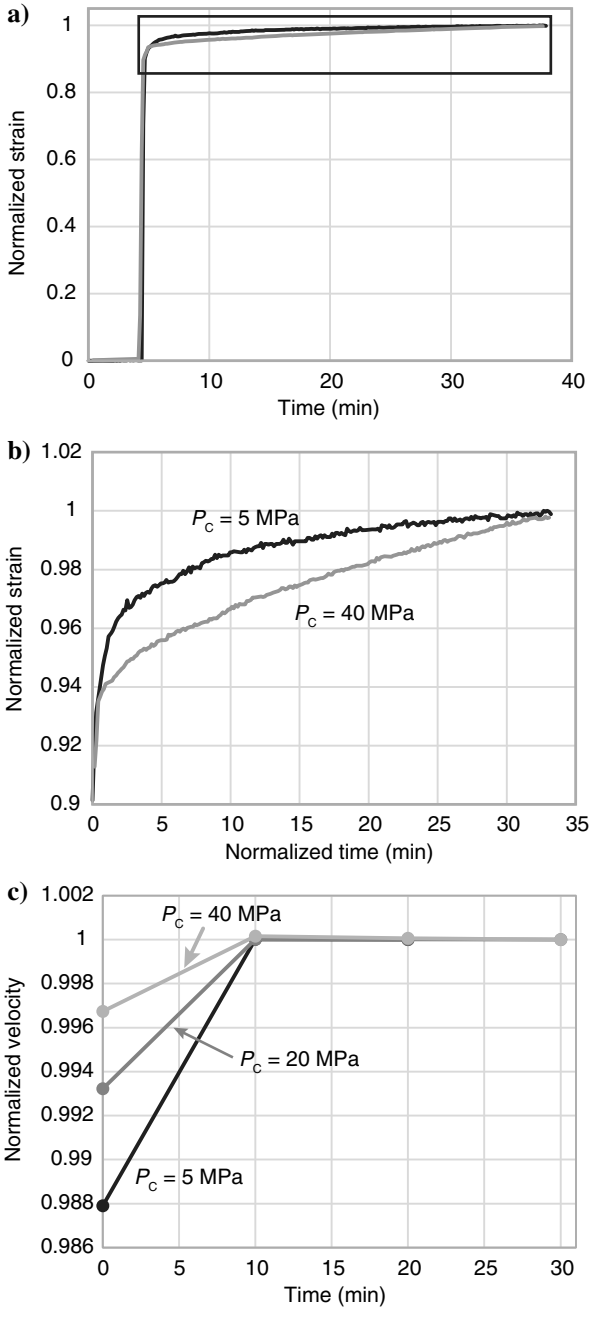

Figure 7. A representative example of the time dependence of strain and velocity during acoustic experiments. (a and b) The evolution of axial strain as a function of time after increasing the confining pressure from 2 to 5 MPa (black) and from 30 to 40 MPa (gray). The strain is normalized to a maximum value of one. The evolution documented in panel (b) is an inset of the box in panel (a). (c) The evolution of velocity as a function of time at 5 (black), 20 (dark gray), and 40 MPa (light gray). In each instance, the *y*-axis is normalized to the ultimately reported value.

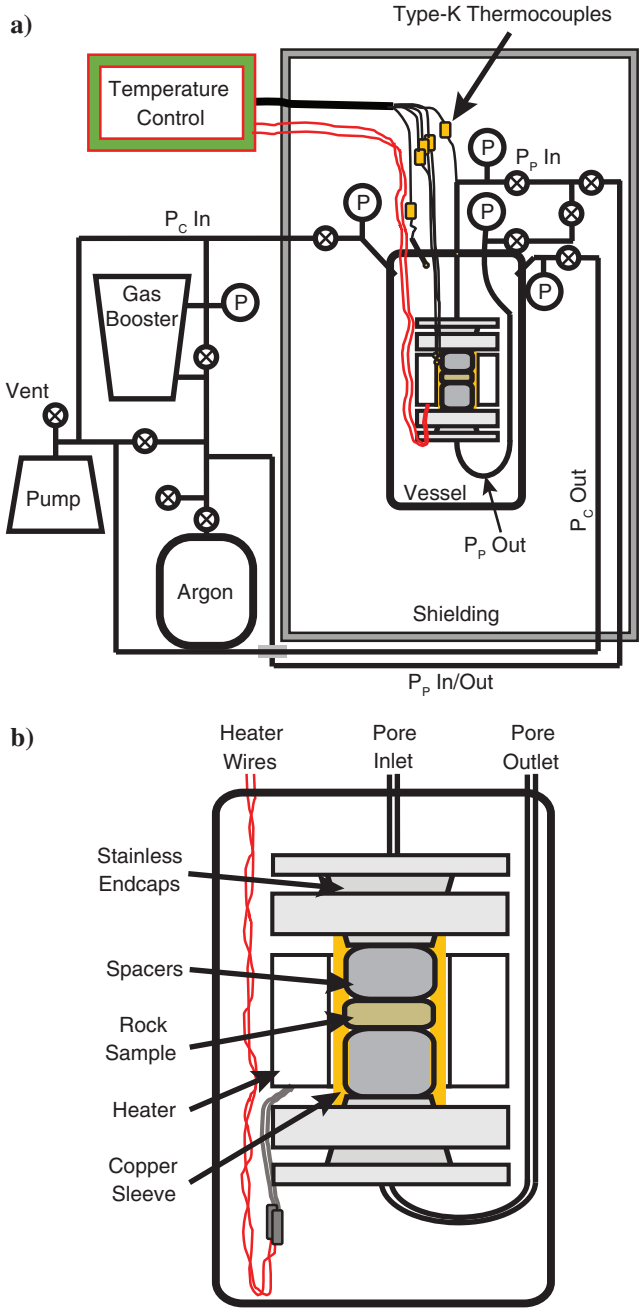

Figure 8. A schematic representation of the HTHP system. (a) Entire system, including core holder, plumbing, and thermal wiring. (b) Enlarged schematic of the composition of the core holder within the pressure vessel.

Complete flow of operations

The iterative characterization of the samples in this study, with multiple experimental methods, results in a complex procedural workflow. For clarity, the full order of operations, including iterative pyrolysis, is documented in Figure 10. Once the pyrolysis experiment is complete and the vessel has cooled, the copper jacket is removed and SEM imaging and porosimetry experiments are conducted on the unjacketed sample. Finally, velocity experiments are performed, as described, on the rubber-jacketed sample. It is important to note that the samples are not re-prepared postpyrolysis. No attempt is made to clean, level, or polish the sample faces, and no oil is flushed/removed from the pore space. The sample is left unaltered postpyrolysis to preserve any maturation-induced textures or visible hydrocarbons for characterization by SEM imaging. It is also important that generated oil is retained in the pore space to enable thermal cracking to gas during subsequent pyrolysis experiments.

RESULTS

Pyrolysis-induced geochemical, physical, and microstructural evolution

Barnett Shale

The geochemical characterization of the Barnett and Green River samples in each window of thermal maturity is reported in Table 4. The Rock-Eval thermal maturity parameter T_{MAX} indicates that pyrolysis at 360°C for 72 h results in early oil window maturity for the Barnett sample (435°C < T_{MAX} < 445°C; Peters and Cassa, 1994). Furthermore, the fourfold increase in free hydrocarbons (S_1) and 45% reduction in remaining hydrocarbon potential confirms that thermal maturation has occurred. However, it is important to note that the subsample used for geochemical characterization exhibited far greater produced oil and hydrocarbon staining and odor than the other Barnett subsamples matured at 360°C. Time-lapse photographs of the sample document the lack of hydrocarbon staining postpyrolysis (Figure 11a and 11b). Further, time-lapse SEM imaging indicates very little alteration of the microstructure after the first pyrolysis experiment (Figure 12a–12d) — we do identify potential compaction in small clay-rich regions, however. Additionally, the sample exhibits a severe decrease in bulk volume (7%) and effective porosity (7.11 p.u.; Table 5). Together, these results indicate that the vertically cored Barnett sample has experienced significant compaction upon pyrolysis to the oil window. Subsequently, given the negligible visible alteration (Figures 11a–11b and 12a–12d), lack of observed hydrocarbons (visual and olfactory), we assume that minimal thermal maturation has occurred in the "oil window" Barnett samples. Rather, the clay matrix has dewatered (hence the mass loss; Table 5) and the fragile, high porosity outcrop sample has been compacted by exposure to high temperature and pressure for three days.

Also note that during pyrolysis to the oil window, the copper seal around the horizontally cored Barnett sample sheared, resulting in equilibration of the confining and pore pressures over a couple of minutes. The rapid depressurization fractured the sample subparallel to the bedding plane to a degree that the sample became unusable (Figure 11d). As a result, the quantitative analysis of the acoustic and elastic evolution of the Barnett Shale is restricted to the vertically cored plug, although a qualitative discussion of the anisotropic evolution is presented in the "Discussion" section. Due to the loss of this plug, SEM images of the horizontal Barnett sample are collected on an additional subsample that was also matured as specified in the "Methods" section. All other SEM images are collected from the velocity subsamples.

Further pyrolysis at 425°C results in postmature, gas window thermal maturity (T_{MAX} > 470°C; Peters and Cassa, 1994; Table 4). The postmature characterization by T_{MAX} is corroborated by an 84%–89% decrease in total remaining hydrocarbon potential and the quantity of hydrocarbons per gram of TOC. Additionally, there is clear evidence of hydrocarbon staining and subparallel to bedding cracking after the second pyrolysis experiment (Figure 11c). Postpyrolysis to the gas window, the organic content of the Barnett Shale exhibits significantly more evolution than in the oil window (Figure 12e and 12f). Although the mineral texture remains largely unaltered, many organic bodies are migrated from the surface into the pore lines, whereas those that remain show significant alteration. Higher resolution images (right column of Figure 12d and 12f) document little residual organic matter; rather, kerogen is almost completely expelled into the pore lines, revealing the underlying mineral matrix and porosity. It is important to note that, these textural evolutions are imaged on the outer surface of the sample, where hydrocarbons are readily expelled from the surface into the pore lines. However, within the core of our sample or in situ, where permeability is sufficiently low, pore pres-

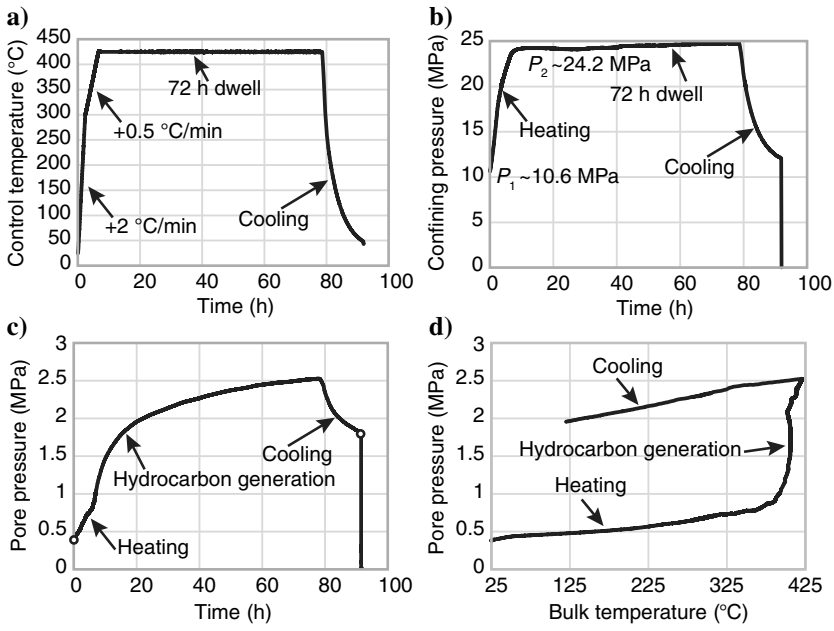

Figure 9. Temperature and pressure monitoring from an example pyrolysis experiment. (a) Temperature of the control thermocouple as a function of time. (b) Confining pressure as a function of time. (c) Pore pressure as a function of time. (d) Pore pressure as a function of the bulk temperature in the reactor (computed from the confining pressure using the ideal gas law). The white circles in panel (c) illustrate the nonthermal expansion-induced pore pressure accumulated during pyrolysis.

sure will build up more than at the surface of our sample; as a result, the in situ textural evolution may differ from that imaged here. Most importantly, physically, the sample exhibits the mass loss, decrease of grain volume, and increase of porosity and grain density indicative of the generation and expulsion of low-density hydrocarbons (Table 5).

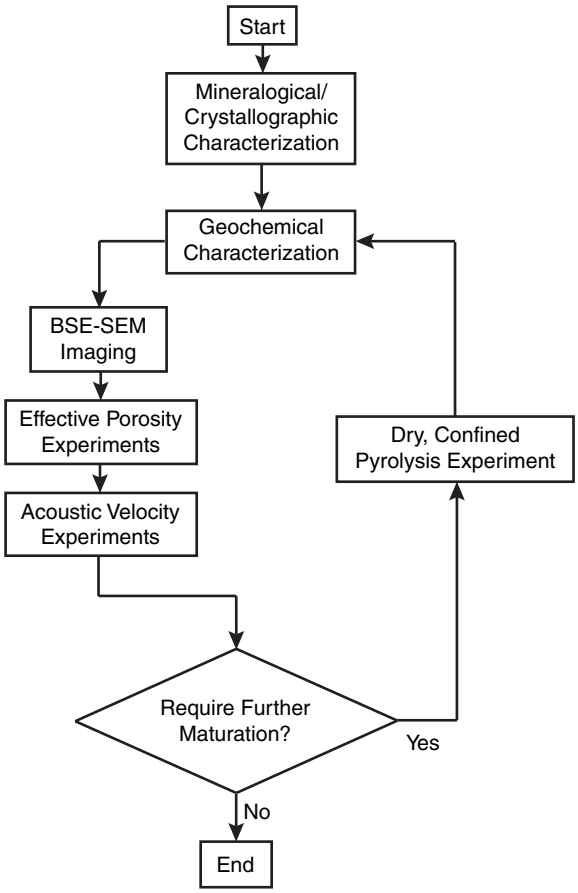

Figure 10. A schematic flowchart of the experimental workflow implemented for iterative shale characterization pre and postpyrolysis. Flowchart modeled on the one originally presented in Allan et al. (2014).

Green River

As a result of the minimal thermal alteration of the Barnett sample, the temperature for oil window pyrolysis experiments of the Green River was raised to 380°C. Table 4 implies that pyrolysis at 380°C resulted in no appreciable maturation of the Green River sample ($T_{MAX} < 435$°C; Peters and Cassa, 1994); however, the presence of hydrocarbons postmaturation was clear for all subsamples (Figure 13), the free hydrocarbons increased by a factor of four, and the remaining hydrocarbon potential decreased by 25%. Microstructurally, the removal of kerogen from the sample is clear (Figure 14). Furthermore, there is an up to 12% decrease in grain

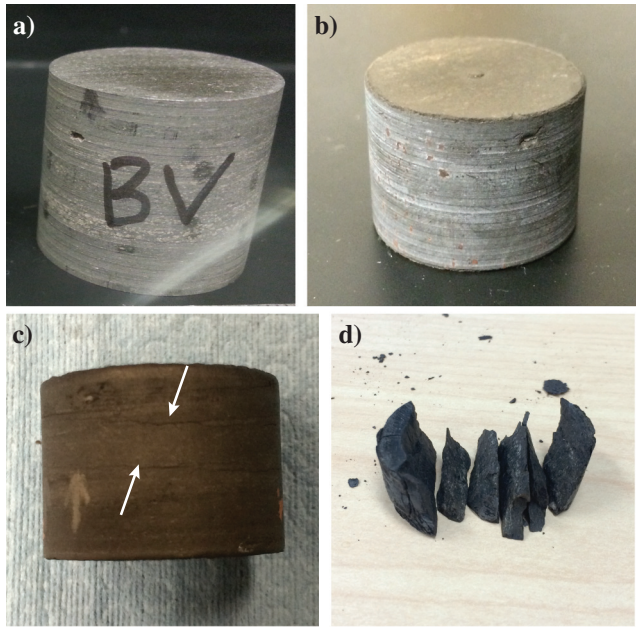

Figure 11. Photographs of the vertically cored Barnett sample in the (a) immature, (b) oil, and (c) gas windows. Also included in panel (d) is the horizontally cored Barnett sample after depressurization during pyrolysis to the oil window. Subparallel to bedding cracks are highlighted for the pyrolyzed gas window sample by white arrows.

Table 5. The physical properties (mass, volume, effective porosity, and grain density) at each stage of thermal maturity.

Sample	Thermal maturity	Mass (g)	Bulk volume (cm^3)	Grain volume (cm^3)	Effective porosity (%)	Grain density (g/cm^3)
Barnett (vertical)	Immature	21.11	10.50 ± 0.02	9.11 ± 0.03	13.23 ± 0.36	2.32 ± 0.01
	Oil	20.70	9.78 ± 0.02	9.18 ± 0.02	6.12 ± 0.44	2.25 ± 0.01
	Gas	20.38	9.44 ± 0.08	8.22 ± 0.01	12.94 ± 0.87	2.52 ± 0.01
Green River (vertical)	Immature	23.10	10.28 ± 0.02	10.23 ± 0.01	0.53 ± 0.48	2.26 ± 0.01
	Oil	21.90	10.07 ± 0.03	8.97 ± 0.02	10.96 ± 0.36	2.44 ± 0.01
	Gas	21.20	10.00 ± 0.06	8.34 ± 0.01	16.55 ± 0.61	2.54 ± 0.01
Green River (horizontal)	Immature	24.40	10.79 ± 0.03	10.65 ± 0.02	1.28 ± 0.32	2.29 ± 0.01
	Oil	23.16	10.71 ± 0.11	9.52 ± 0.03	11.13 ± 1.08	2.43 ± 0.01
	Gas	21.93	10.50 ± 0.10	8.39 ± 0.01	20.11 ± 0.98	2.61 ± 0.01

volume and a tenfold increase in porosity indicative of the conversion of low-density kerogen to hydrocarbons and their subsequent expulsion (Table 5). Subsequently, given the clear visual kerogen conversion, significant increase in grain density, and the retention of oil for all Green River subsamples, we assume they have entered the oil window.

Pyrolysis at 425°C results in a postmature, gas window horizontally cored Green River sample ($T_{MAX} > 470$°C; Peters and Cassa, 1994). However, the vertically cored Green River sample exhibits an anomalously low thermal maturity value representative of an early oil window sample (435°C < T_{MAX} < 445°C; Peters and Cassa, 1994) and 3.8 times more residual hydrocarbons by weight than the horizontally cored plug. At the same time, the remaining thermally producible hydrocarbons (S_2) have decreased by 90% and 82% as compared with the baseline and oil window values (Table 4), respectively. Subsequently, it appears that, again, the sample has thermally matured, but there is some error associated with the reported value of T_{MAX}. Although the hydrocarbon staining of the sample is clear (Figure 13), there is very little thermally dependent microstructural evolution of the Green River samples postpyrolysis to the gas window (Figure 15). During pyrolysis to the oil window, the majority of the visible kerogen was expelled from the imaged surface of the sample into the pore lines; subsequently, there is little kerogen evolution to observe. It is important to remember that SEM is largely restricted to a 2D surface; thus, the thermal maturation and porosity generation indicated in Table 5 can only be inferred to occur within the 3D sample. Finally, we also observe largely randomly oriented microcracking between and within grains (Figure 15) postpyrolysis.

It is important to note that the formation of CO_2, H_2S, and organic acids during thermal maturation may contribute to the large increase in porosity in the Green River samples (Table 5) by dissolving carbonate minerals. However, through SEM imaging, we observe no dissolution, smoothing of grain contacts/edges, or etching/pitting indicative of carbonate dissolution (Figures 14 and 15). Subsequently, we attribute the large increase in porosity predominantly to the conversion and expulsion of the pore-filling kerogen.

Acoustic velocity and elastic anisotropy results

Baseline immature window

The P- and S-wave velocities as a function of confining pressure for both orientations of immature samples are documented in Figure 16. As expected for an assumed vertically transversely isotropic (VTI) medium, the vertically propagating P-waves are significantly slower and more pressure-sensitive than those propagating horizontally in the laminar Barnett Shale sample. The Barnett sample exhibits additional velocity relationships expected for a VTI medium; for instance, the $V_S(0°)$ and $V_{SV}(90°)$ phases are roughly equal with magnitude significantly less than $V_{SH}(90°)$. Any similar VTI behavior present in the Green River sample is severely suppressed. The directional dependence of P- and S-wave velocities is minimal in comparison with the directional dependence of the Barnett samples. Further, there exists a considerably lesser degree of agreement between the $V_S(0°)$ and $V_{SV}(90°)$ phases of the Green River sample. Finally, all phases of the Green River sample are less sensitive to pressure than the corresponding acoustic phase of the Barnett sample.

Given the difference in the directional dependence of the acoustic velocities of the two samples, it is understandable that the samples exhibit significantly different elastic anisotropies (Figure 17). The strong directional dependence of P- and S-wave velocities in the laminar Barnett Shale sample gives rise to significant, pressure-sensitive elastic anisotropy. The P-wave velocities and epsilon are considerably more pressure-sensitive than the S-wave velocities and gamma, as previously discussed by MacBeth (2004). The relative lack of directional dependence or pressure-sensitivity in the acoustic velocities of the interlocking carbonate structure of the Green River sample, contrastingly, results in a low degree of elastic anisotropy, which is largely insensitive to pres-

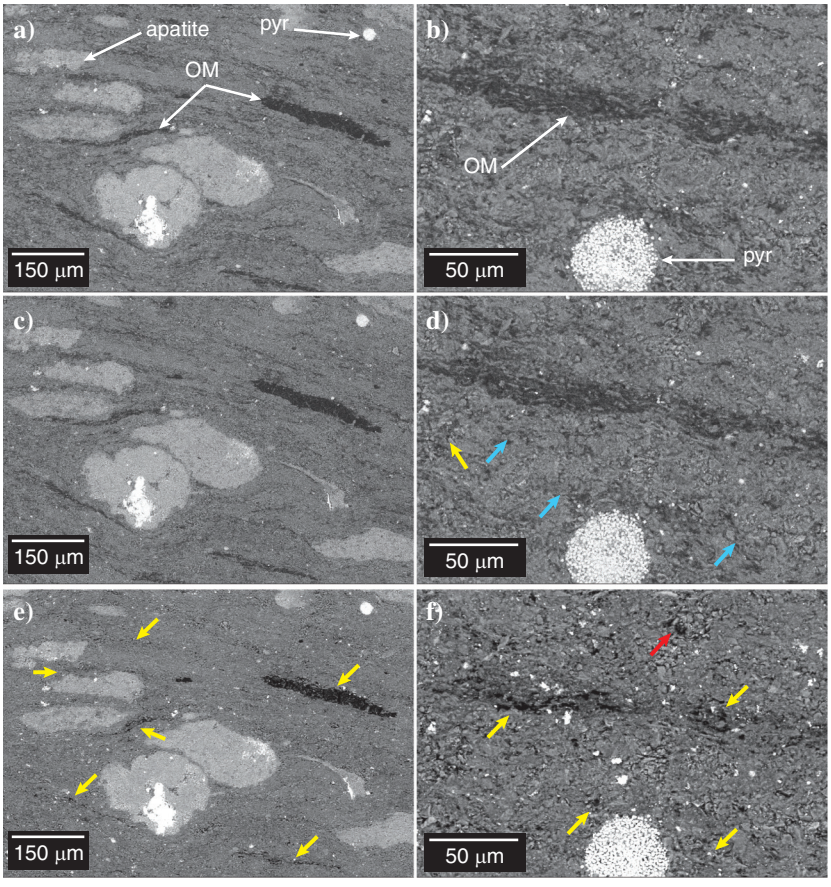

Figure 12. Time-lapse SEM images of the evolving microstructure of two regions of the (a and b) initially thermally immature Barnett Shale sample. The same locations are also shown in the (c and d) oil window and (e and f) gas window. Identified features include organic matter (OM), pyrite (pyr), and apatite. Evolutions noted include: blue arrows identifying potential compaction in clay-rich regions, red arrows identifying areas of cracking or developing porosity, and yellow arrows identifying areas of kerogen conversion and expulsion. The pixel size in each series of time-lapse images is identical.

sure. For convenience, all velocity and anisotropy results at 50 MPa confining pressure are reported in Table 6.

Oil window

The vertically propagating P- and S-wave velocities for the oil window Barnett Shale sample are reported in Figure 18. After pyrolysis to the oil window, the velocities increase relative to the baseline values — P: 510 m/s (20%), S: 180 m/s (10%) at 50 MPa, significantly greater than the experimental error of 1%. The velocity increase in the Barnett velocities corresponds with a decrease in effective porosity from 13.23% to 6.12% at room temperature and pressure (Table 5). The oil window Green River velocities are documented as a function of confining pressure in Figures 19 and 20. All acoustic velocities exhibit a decrease in magnitude and an increase in pressure sensitivity postpyrolysis, whereas the effective porosity of the vertical and horizontal plugs increases from 0.53% and 1.28% to 10.96% and 11.13% (Table 5), respectively. Pyrolysis to the oil window results in a decrease in P-wave velocities of 9% and 8% for the vertical and horizontal plugs (Figure 19), respectively, and a decrease in the S-wave velocities of 4.5%, 5%, and 3%, for the $V_S(0°)$, $V_{SH}(90°)$, and $V_{SV}(90°)$ phases (Figure 20), respectively. Again, the experimental error in velocity measurements is 1%.

In Figure 21, the Green River sample is shown to exhibit very little change in epsilon postpyrolysis to the oil window. Similarly, the value of gamma does not change significantly (± 0.03), with a notable decrease (-0.04) in gamma as a function of confining pressure resulting from the greater pressure-sensitivity of the $V_{SV}(90°)$ phase relative to $V_{SH}(90°)$.

Gas window

After pyrolysis to the gas window, all remaining samples were recovered with no visible damage. The gas window P- and S-wave velocities perpendicular to bedding for the Barnett Shale sample are documented in Figure 18. Postpyrolysis to the gas window, the Barnett Shale velocities are greatly more sensitive to confining pressure. In the gas window, the P- and S-wave velocities increase by 30% and 14% upon loading to 20 MPa, respectively. However, at confining pressures greater than 20 MPa, the gas window velocity-pressure trend conforms well to the oil window trend: indeed, the high confining pressure velocities show no significant difference (± 30 m/s). The two trends remain in close agreement during unloading until approximately 5 MPa, below which the gas window sample becomes more sensitive to confining pressure. As in the oil window, the Green River P- and S-wave velocities exhibit a significant decrease at all confining pressures and an increase in the pressure-sensitivity of velocity (Figures 19 and 20). Upon pyrolysis to the gas window, the P-wave velocities experience a further decrease of 9% and 7% for the vertical and horizontal plugs (Figure 19), respectively, and a decrease in the S-wave velocities of 5.5%, 10%, and 19%, for the $V_S(0°)$, $V_{SH}(90°)$, and $V_{SV}(90°)$ phases (Figure 20), respectively.

The evolution of the elastic anisotropy of the Green River is documented in Figure 21. The values of epsilon show a slight ($+0.02$) increase upon pyrolysis to the gas window, with a very small degree

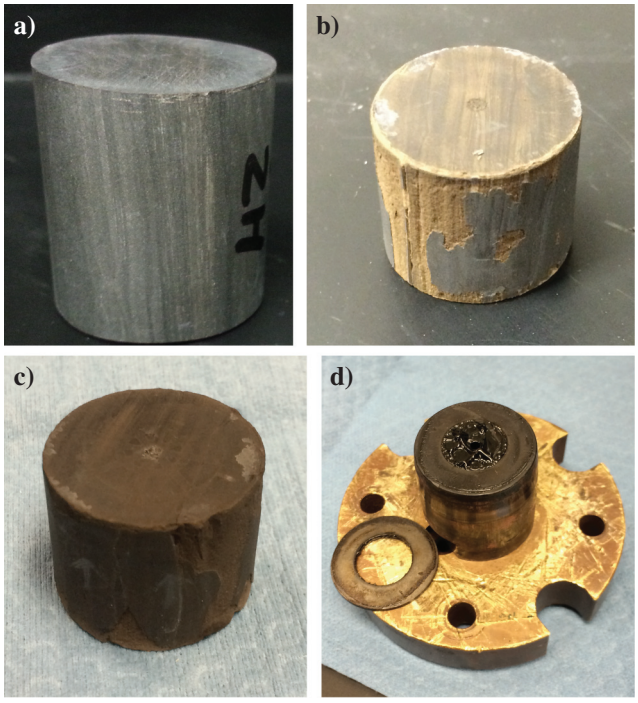

Figure 13. Photographs of the horizontally cored Green River sample in the (a) immature, (b) oil, and (c) gas windows. Also included in panel (d) is the steel endcap postpyrolysis to the oil window documenting clear oil generation.

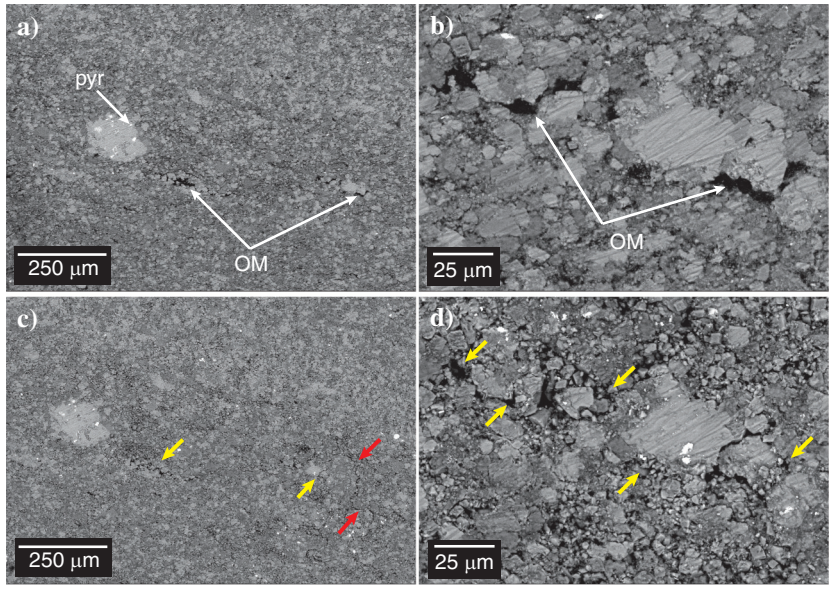

Figure 14. Time-lapse SEM images of the evolving microstructure of two regions of the (a and b) initially thermally immature Green River sample. (c and d) The same locations are also shown in the oil window. Identified features include organic matter (OM) and pyrite (pyr). Evolutions noted include: red arrows identifying areas of cracking or developing porosity and yellow arrows identifying areas of kerogen conversion and expulsion. The pixel size in each series of time-lapse images is identical.

of pressure-sensitivity (−0.04) — particularly evident upon unloading. The gas window values of gamma exhibit a significant increase in magnitude (approximately a factor of three increase), with a small (+0.02) increase with confining pressure.

DISCUSSION

Elastic evolution with increasing thermal maturity

Barnett Shale

After the first pyrolysis experiment, the vertically propagating P- and S-waves exhibit an increase of 510 (19%) and 180 m/s (10%) at 50 MPa confining pressure, respectively (Figure 18). This velocity increase is sensible given the 54% (7.11 p.u.) decrease in the unsaturated effective porosity resulting from the 7% decrease in bulk volume for an effectively constant grain volume sample (Table 5). The combination of the previously observed lack of hydrocarbon production, decrease in bulk volume and effective porosity, and the significant increase in acoustic velocity are all indicative of the mechanical compaction of the thermally softened sample.

Given the potential for such significant compaction in weak, clay-rich outcrop samples, it would be advantageous for future ex-

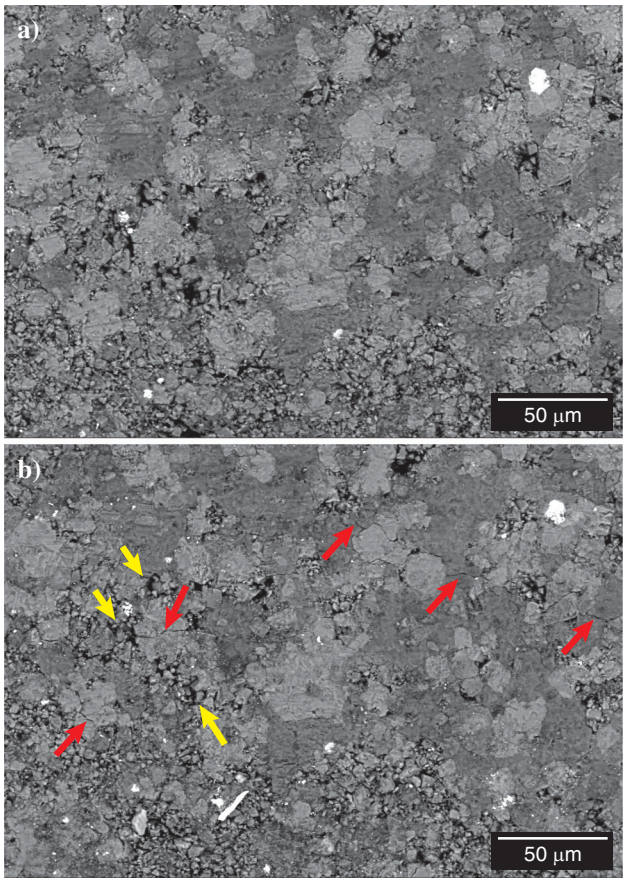

Figure 15. Time-lapse SEM images of the evolving microstructure from the (a) oil window to the (b) gas window of the Green River sample. Evolutions noted include: red arrows identifying areas of cracking or developing porosity and yellow arrows identifying areas where previously organic voids have been compacted. The pixel size in each image is identical.

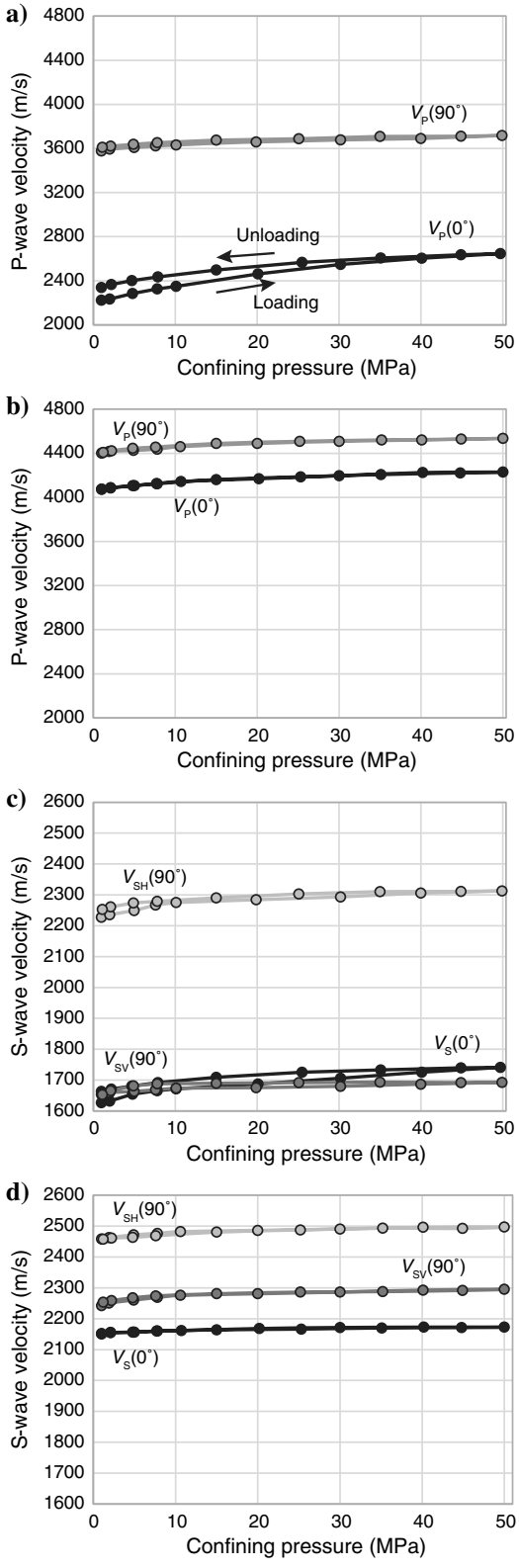

Figure 16. (a and b) The baseline, immature P- and (c and d) S-wave velocities as a function of confining pressure for the (a and c) Barnett and (b and d) Green River samples. Solid lines and arrows are used to indicate hysteresis between the loading and unloading curves.

periments that all samples be thermally prestressed before baseline characterization. By exposing the samples to high pressure and intermediate temperatures (sufficient to soften the sample, but not so hot as to induce thermal maturation, e.g., 300°C) for a few days, any potential mechanical compaction will be accounted for before the baseline, thermally immature measurements are taken. As a result, all future observed evolutions should be more purely a function of thermal maturation. However, this prestressing technique may result in the premature dewatering of the sample — a deviation from the saturated, potentially overpressured nature of thermally maturing organic-rich shale in situ. As a result of this deviation, the organic evolution and developed textures may differ from those observed in nature. The issues of balancing significant compaction and premature dewatering can be addressed in future work by comparing pyrolyzed samples from the same horizon, one of which has been prestressed, while the other is preserved as received. Such experiments are a necessary component of establishing best practices for the pyrolysis of clay- and organic-rich rocks.

Due to this lack of hydrocarbon generation in the first pyrolysis experiment, we can consider the "oil window" velocities as an updated baseline characterization. At low-confining pressure, postpyrolysis to the gas window, there is a decrease in the P- and S-wave velocities of 375 (13%) and 130 m/s (7%), respectively (Figure 18). As the hydrostatic confining pressure is increased from 1 to 20 MPa, the acoustic velocities increase rapidly — up to twice the rate of the oil window velocities. The extreme pressure sensitivity of the P- and S-wave velocities is further evidence of the previously imaged subparallel to bedding cracks (Figure 11). Notably, upon the closure of the induced cracks at confining pressures greater than 20 MPa, the pre and postpyrolysis samples become acoustically indistinguishable to P- and S-waves.

Due to the fracturing of the horizontally cored Barnett Shale sample during pyrolysis to the oil window, it is impossible to directly quantify the elastic anisotropy of the Barnett Shale upon pyrolysis. However, by applying a set of restrictions to the evolution of the horizontally cored sample, we can establish hypothetical horizontal velocity values and qualitatively comment on the resultant elastic anisotropy. To define the evolution of the horizontal plug postpyrolysis, we make the following observations and assumptions:

- Postpyrolysis, the vertically cored plug exhibits subparallel to bedding cracking; we assume that the horizontally cored plug would also preferentially crack in this orientation.
- The Kimmeridge Shale samples of Allan et al. (2014) are of similar clay content and are similarly textured to the Barnett Shale sample; further, the Kimmeridge samples also exhibit subparallel to bedding cracking.
- Upon pyrolysis, the vertically propagating Kimmeridge P-wave velocity decreased by 17.8%, whereas the horizontally propagating P-wave velocity decreased by only 1.2%.

Subsequently, we assume that, as with the Kimmeridge shale, the acoustic velocities of the horizontally cored Barnett plug will evolve negligibly compared with the vertically cored plug. Thus, we can estimate the elastic anisotropy of the Barnett shale by holding the horizontally propagating velocities constant as a function of thermal maturity. It is important to note that by assuming no evolution of the horizontal velocities postpyrolysis, we likely calculate the maximum possible anisotropic evolution with thermal maturity. If, in reality, the horizontal velocities of the more porous pyrolyzed plug decrease, the true values of epsilon will be lower than those estimated here; further, it is highly unlikely that the horizontal velocities will increase given the noted 6–7 p.u. increase in unsaturated effective porosity postpyrolysis.

The change in anisotropy upon pyrolysis to the gas window (for some anisotropic parameter ψ) is then

$$\Delta\psi = \psi_{\text{post}} - \psi_{\text{pre}}, \tag{8}$$

where for epsilon, ψ_{post} may be written as

$$\begin{aligned}\varepsilon_{\text{post}} &= \left(\frac{C_{11}-C_{33}}{2C_{33}}\right)_{\text{post}} \\ &= \left(\frac{\rho_{B,\text{gas}}(V_{\text{P,gas}}(90°))^2 - \rho_{B,\text{gas}}(V_{\text{P,gas}}(0°))^2}{2\rho_{B,\text{gas}}(V_{\text{P,gas}}(0°))^2}\right).\end{aligned} \tag{9}$$

The same process may then be followed for gamma using the standard definitions from equations 4, 5, and 7. The change in anisotropy upon pyrolysis to the gas window (as defined in equation 8) is presented in Figure 22. For epsilon and gamma, we see that postpyrolysis, the induced subparallel to bedding microcracks result in an increase in the magnitude of elastic anisotropy due to the slowing of the vertically propagating acoustic waves. However, with increasing confining pressure, as the observed microcracks close, epsilon and gamma return, approximately, to their prepyrolysis values. Subsequently, under the aforementioned assumptions, the thermal maturation of laminar shale is only anisotropically observable as long as the generated hydrocarbons are retained and propping open the induced, subparallel to bedding cracking. The expulsion or migration of these fluids would allow the cracks to close and the anisotropic contrast with the thermally immature shale to be lost.

Table 6. Database of measured acoustic velocities and derived Thomsen anisotropy parameters for dry samples at a hydrostatic confining pressure of 50 MPa.

Sample	Thermal maturity	Velocity (m/s)					Anisotropy	
		$V_{\text{P}}(0°)$	$V_{\text{P}}(90°)$	$V_{\text{S}}(0°)$	$V_{\text{SV}}(90°)$	$V_{\text{SH}}(90°)$	Epsilon	Gamma
Barnett	Immature	2646	3717	1726	1693	2313	0.486	0.434
	Oil	3153	—	1921	—	—	—	—
	Gas	3126	—	1932	—	—	—	—
Green River	Immature	4229	4528	2171	2292	2497	0.079	0.092
	Oil	3856	4181	2076	2229	2371	0.085	0.066
	Gas	3518	3891	1959	1797	2129	0.102	0.202

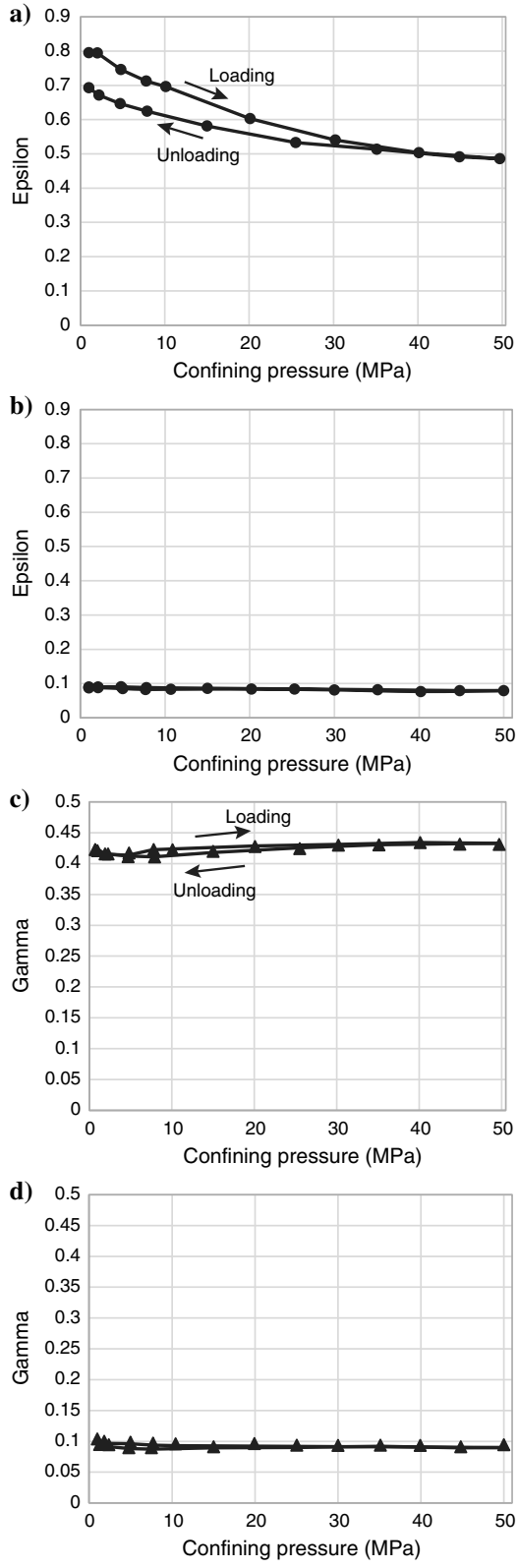

Figure 17. The calculated Thomsen anisotropy parameters (a and b) epsilon and (c and d) gamma as a function of confining pressure for the (a and c) Barnett and (b and d) Green River samples. Solid lines and arrows are used to indicate hysteresis between the loading and unloading curves.

Green River

The acoustic response of the Green River samples to pyrolysis to the oil window is documented in Figures 19 and 20. As previously noted, the decrease in velocity is sensible given the sizeable (approximately 10 p.u.) increase in unsaturated effective porosity. The increase in velocity sensitivity to pressure is further an indication of the conversion to fluids and expulsion of load-bearing, pore-filling organic matter during pyrolysis. Most notably, however, is that the velocity decrease in the oil window is effectively isotropic, with the directional dependence being no greater than 60 m/s for any acoustic phase. This indicates that there is no appreciable development of aligned compliant porosity or other aligned features during pyrolysis to the oil window. Rather, combined with the noted mass loss and increase in effective porosity, as well as grain density between the two plugs (Table 5), the Green River samples appear to evolve uniformly and isotropically.

Upon thermal maturation to the gas window, the unsaturated effective porosity of the vertical and horizontal plugs increases by a further 6 and 10 p.u., respectively; subsequently, there is a 7%–9% and 6%–19% decrease in the P- and S-wave velocities. The generation and expulsion of additional hydrocarbons also result in an increase in the pressure-sensitivity of the acoustic velocities. Again, we see that the evolution of P-wave velocities postpyrolysis is

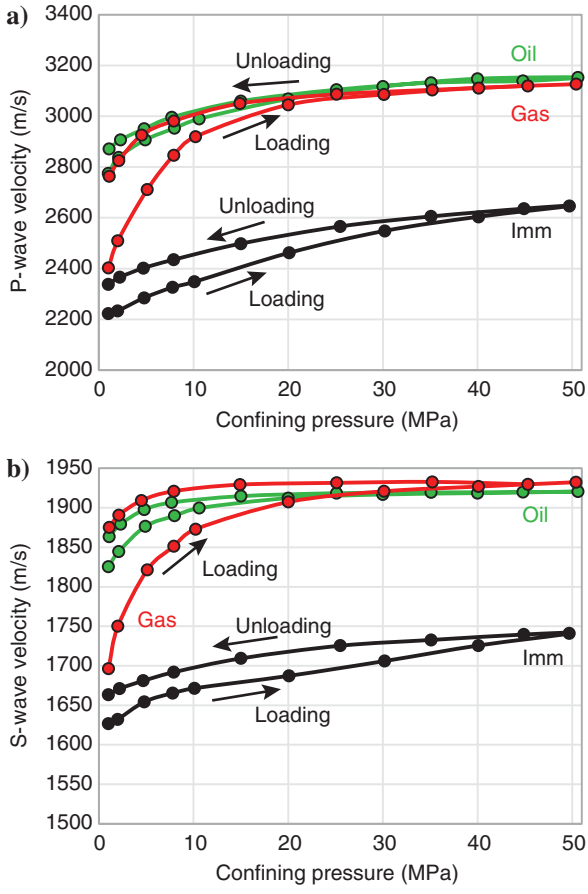

Figure 18. The vertically propagating (a) P- and (b) S-wave velocities of the Barnett Shale sample in the immature (black), oil (green), and gas (red) windows. Solid lines and arrows are used to indicate hysteresis between the loading and unloading curves.

largely isotropic, indicative of limited induced alignment or aligned microcracking. However, there does exist a significant directional dependence of shear velocities postpyrolysis. The greater velocity of vertically propagating S-waves is most likely a function of 3.8 times greater quantity of retained hydrocarbons in the vertically cored sample.

The negligible evolution of epsilon (±0.02) between the thermally immature and oil windows for the Green River sample is representative of the previously noted largely isotropic evolution of P-wave velocities (Figures 19 and 21). Note that the calculated values of epsilon for two orthogonally cored plugs assume that the plugs are homogeneous. However, the density and effective porosity of the two Green River core plugs are not completely homogeneous (Table 5), particularly in the gas window due to differential bitumen/hydrocarbon retention (Table 4). Thus, the reported values of epsilon may reflect the effect of this heterogeneity.

Contrastingly, gamma is defined by velocities measured exclusively on the horizontal plug, thus no such heterogeneity exists. In the oil window, the high confining pressure values of gamma are 28% lower than the prepyrolysis values due to a greater decrease in $V_{SH}(90°)$ compared with $V_{SV}(90°)$ (Figures 20 and 21). The developed pressure-sensitivity of gamma arises from the greater pressure sensitivity of $V_{SV}(90°)$. Although this increase in pressure-sensitivity is indicative of compliant features aligned with the bedding plane, the greater magnitude decrease in $V_{SH}(90°)$ relative to $V_{SV}(90°)$ (Figure 20) and lack of observed aligned cracking (Figures 13 and 14) indicate that microcracks are not the source of this pressure-sensitivity. We lack the necessary X-ray microtomography data to resolve any possible aligned features within the sample; however, the magnitude of the pressure-sensitivity (±0.04) is

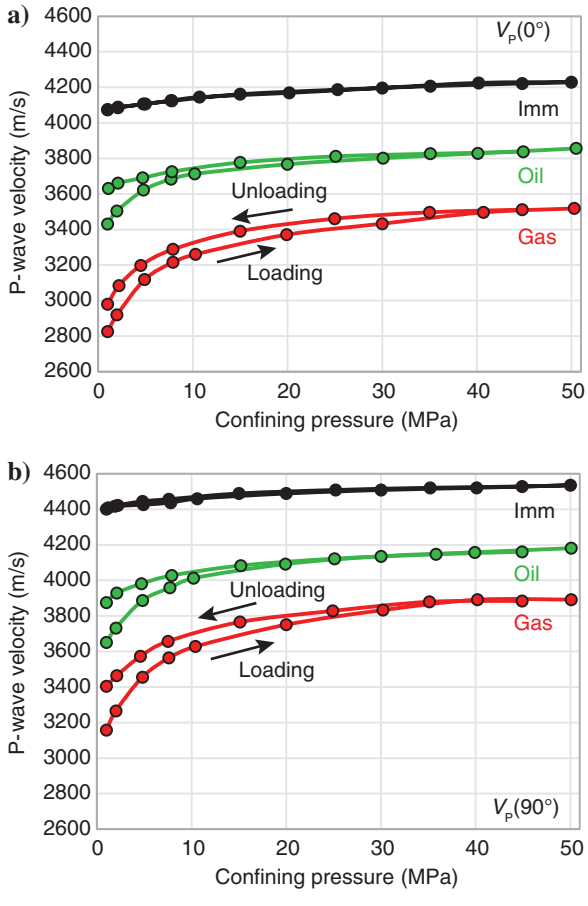

Figure 19. The P-wave velocities of the Green River sample, (a) perpendicular and (b) parallel to bedding, in the immature (black), oil (green), and gas (red) windows. Solid lines and arrows are used to indicate hysteresis between the loading and unloading curves.

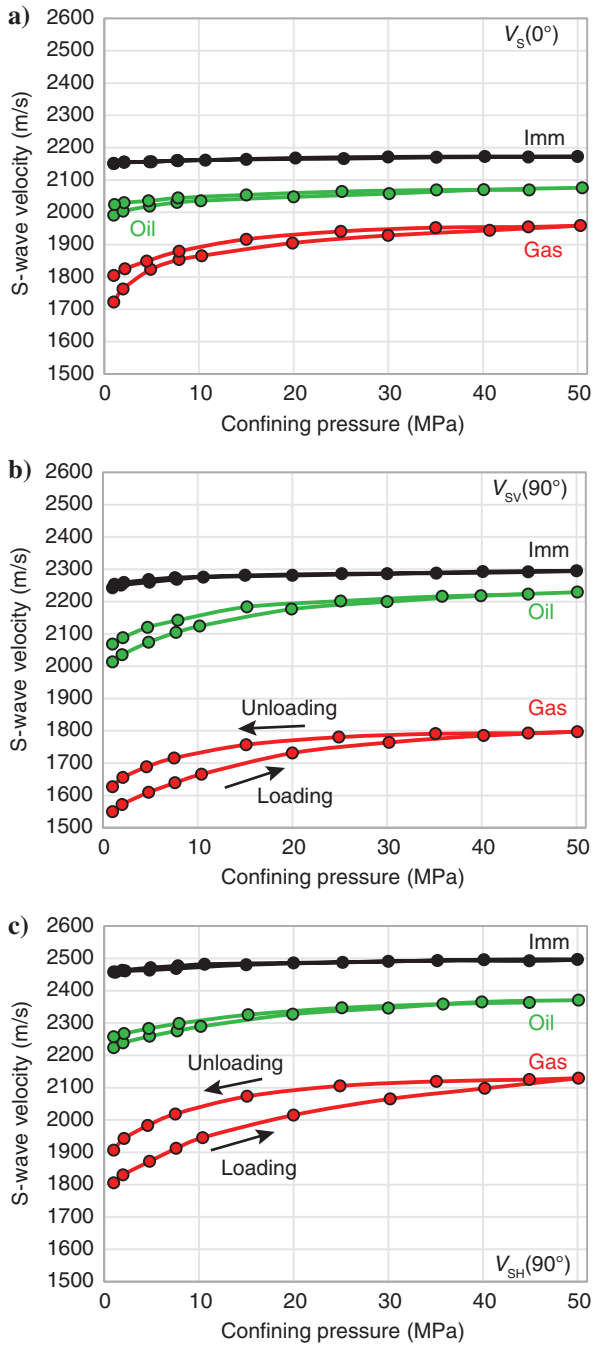

Figure 20. The S-wave velocities of the Green River sample in the immature (black), oil (green), and gas (red) windows. S-wave phases shown are: (a) $V_S(0°)$, (b) $V_{SV}(90°)$, and (c) $V_{SH}(90°)$. Solid lines and arrows are used to indicate hysteresis between the loading and unloading curves.

very low relative to previously studied pyrolyzed samples (Allan et al., 2014, 2015) indicating that microcracking within the sample, if any, is negligible.

After further pyrolysis to the gas window, the high confining pressure value of epsilon again shows very little change (±0.02; Figure 21). The small pressure-sensitivity of epsilon (±0.04) evident in the unloading curve is attributable to the greater hysteresis exhibited by the horizontal sample, which, given the small magnitude of the change, is likely an effect of the previously discussed heterogeneity between the two plugs used to compute epsilon (Table 5).

The values of gamma, in the gas window, increase by a factor of three and exhibit a negligible (±0.02) sensitivity to confining pressure (Figure 21). The increase in the magnitude of gamma results from the much greater decrease in $V_{SV}(90°)$ relative to $V_{SH}(90°)$ — 430 m/s (19%) versus 240 m/s (10%), whereas the small increase in gamma with confining pressure results from the slightly greater pressure-sensitivity of $V_{SH}(90°)$ relative to $V_{SV}(90°)$. The combination of a greater magnitude decrease in $V_{SV}(90°)$ and a greater pressure-sensitivity of $V_{SH}(90°)$ is, again, not indicative of aligned microcracking, in which case, we would expect $V_{SV}(90°)$ to exhibit the greater decrease and pressure-sensitivity.

The changes in gamma across the oil and gas windows document a complex pattern of evolution rather than a simple process, such as the development of microcracks. Ideally, we would have X-ray microtomographic images to illustrate textural evolutions within the sample; however, the geochemical analysis does document a key evolution in the sample. In the oil window, there is a large quantity of generated hydrocarbons retained within the sample (S_1 = 19.25 mg/g; Table 4); by the gas window, the quantity of hydrocarbons retained decreases by 83%. Given the absence of clear microcracking or the development of other aligned features, visually (Figures 13–15) and acoustically (Figures 19–21), the complex behavior of gamma with thermal maturity may be attributable to changes in the quantity and distribution of retained hydrocarbons. This effect may be suppressed in epsilon due to the heterogeneous retention of hydrocarbons associated with the two plugs used to characterize epsilon (Table 4).

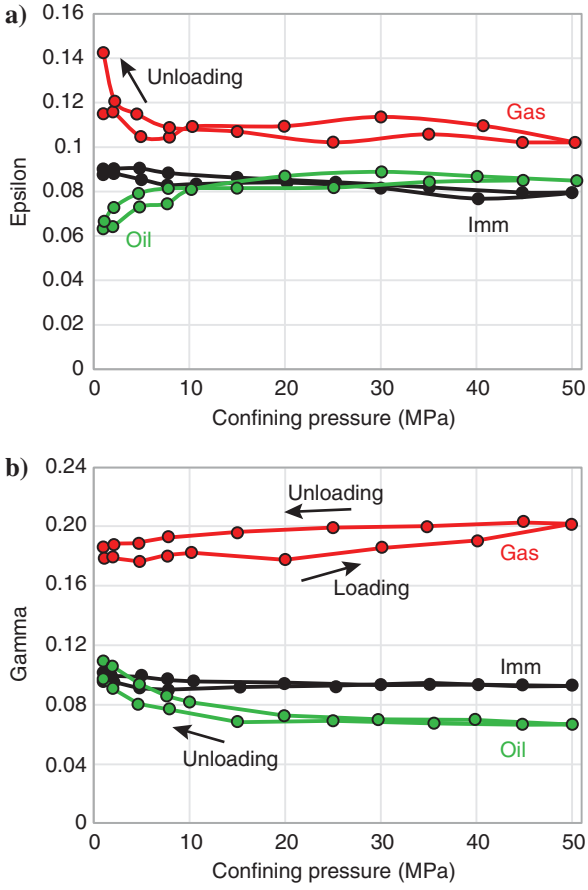

Figure 21. The calculated Thomsen anisotropy parameters (a) epsilon and (b) gamma of the Green River sample in the immature (black), oil (green), and gas (red) windows. Solid lines and arrows are used to indicate hysteresis between the loading and unloading curves.

Phenomenological conceptual models of shale evolution

Barnett Shale

By combining microstructural observations and acoustic velocity measurements, we are able to develop two conceptual models for

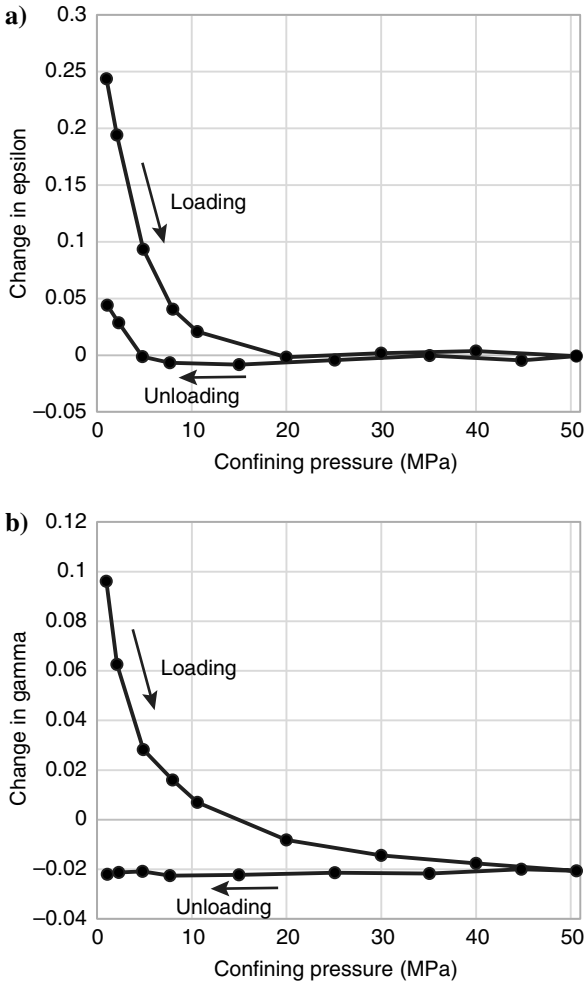

Figure 22. The hypothetical change in (a) epsilon and (b) gamma upon pyrolysis to the gas window for the Barnett Shale sample. Solid lines and arrows are used to indicate hysteresis between the loading and unloading curves.

the phenomenological evolution of organic-rich laminar shale and weakly aligned, micritic samples as a function of thermal maturity. If given, the visual, physical, and geochemical evidence, we consider that little thermal maturation occurred in the Barnett Shale sample during the first pyrolysis experiment; then, we may consider the "oil window" properties as the baseline for any thermal maturity-dependent discussion. Subsequently, prepyrolysis, the laminar Barnett sample is composed of a well aligned, clay-rich matrix with dispersed stiffer grains (apatite) and soft, organic inclusions (Figures 4 and 23). In this model, the vertically propagating acoustic waves exhibit pressure-sensitivity as the application of confining stress results in the partial compaction of the sizeable pore space ($\varphi \sim 13\%$) and soft kerogen inclusions. Postpyrolysis, the mineral matrix remains largely unchanged (Figure 12); however, the organic inclusions have been expelled leaving largely porous voids (Figures 12 and 23). Furthermore, the expulsion of produced hydrocarbons from the thermally decomposing organic lenses, preferentially along the weak bedding planes, results in the formation of subparallel to bedding microcracks (Figure 23). This development of microcracks results in a significant decrease in the acoustic velocities at low confining pressures (Figure 18), i.e., when the microcracks are open. However, the application of increasing confining pressure closes the compliant microcracks, which stiffens the rock frame and increases the acoustic velocities (Figures 18). At high confining pressure, we observe that the acoustic velocity exhibits negligible evolution from the prepyrolysis values. The equivalence of velocity pre and postpyrolysis indicates that the nature of the compliant inclusions; e.g., kerogen-filled or oil-filled or porous, is irrelevant to the load-bearing structure of the composite shale. Subsequently, in this laminar shale model, at low-confining pressure, the acoustic velocity is determined by induced microcracks, whereas at elevated confining pressure, it is the thermally unaltered, load-bearing siliciclastic matrix that determines the acoustic velocity, while the material filling the dispersed compliant inclusions has no appreciable effect on the acoustic response of the rock. In this manner, the thermal maturation of laminar shale is only acoustically observable so long as the induced, subparallel to bedding microcracks are open. Once the generated fluids migrate from the host rock, unless the fluid is immediately replaced by other generated fluids, the cracks are expected to close and the acoustic signature of elevated thermal maturity will be lost.

Importantly, this conceptual model also appears applicable to the Kimmeridge shale samples presented in Allan et al. (2014). The laminar Kimmeridge samples exhibit the same development of cracks, albeit with a wider aperture, and decrease in vertically propagating velocities as seen in the Barnett Shale. However, due to the lack of applied confining pressure during pyrolysis in Allan et al. (2014), the effect of these microcracks is compounded by the formation of sample-scale fractures. These fractures do not close at high confining pressure, as a result, the high confining pressure elastic behavior of the two laminar shales diverges. However, given the similar physical, geochemical, and low pressure elastic evolution of the two shales, we hypothesize that, were the Kimmeridge samples pyrolyzed under applied confining pressures, the high confining pressure behavior of the two laminar shales would be very similar.

Green River

The baseline, thermally immature Green River sample used in this study is a tight (approximately 1% effective porosity), weakly aligned, dolomicrite rather than a "typical" shale (Figure 4). The organic matter occurs in the Green River sample not as discrete, aligned lenses, but rather as an unstructured pore-filling phase. Subsequently, the sample is modeled as a subspherical granular pack with organic matter filling the intergranular pore space (Figure 24). This low porosity morphology with load-bearing, pore-filling kerogen results in fast, largely pressure-insensitive acoustic velocities (Figure 16). Postpyrolysis, the visible loss of kerogen (Figure 14) and increase in effective porosity (Table 5) removes load-bearing pore-fill and results in a significant decrease in acoustic velocities (Figures 19 and 20). Indeed, further pyrolysis amplifies this effect as still more load-bearing pore-fill (in this case, kerogen and heavier hydrocarbons) is expelled and the rock becomes acoustically still slower (Figures 19 and 20). Furthermore, the loss of pore-filling material enables the rock to strain to a greater degree under increasing confining pressure (Figure 24), which is acoustically visible as an increase in the pressure-sensitivity of velocities postpyrolysis. That the acoustic evolution is largely isotropic (Figures 19 and 20), with no noticeable development of aligned compliant features or microcracks, indicates that in the absence of aligned features (e.g., mineral crystals, strong bedding, or organic lenses) in the baseline, thermally immature microstructure, the thermal maturation-induced evolution will occur as a largely uniform, isotropic process. As seen in the previous section, complex anisotropic changes can exist, although the textural source of these changes is not definitively identified. Thus, in this model, the progression of thermal maturation across a horizon in a weakly aligned rock, such as micrites or siltstones, may be visible through lateral decreases in measured

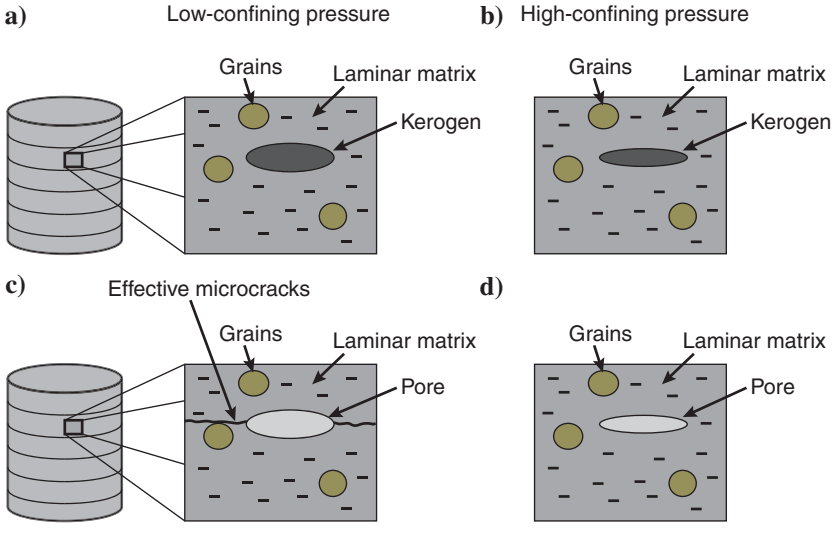

Figure 23. The conceptual model for laminar shale evolution upon thermal maturation as a function of confining pressure. Four stages of evolution are shown: (a) immature sample at low confining pressure, (b) immature sample at high confining pressure, (c) gas window sample at low confining pressure, and (d) gas window sample at high confining pressure.

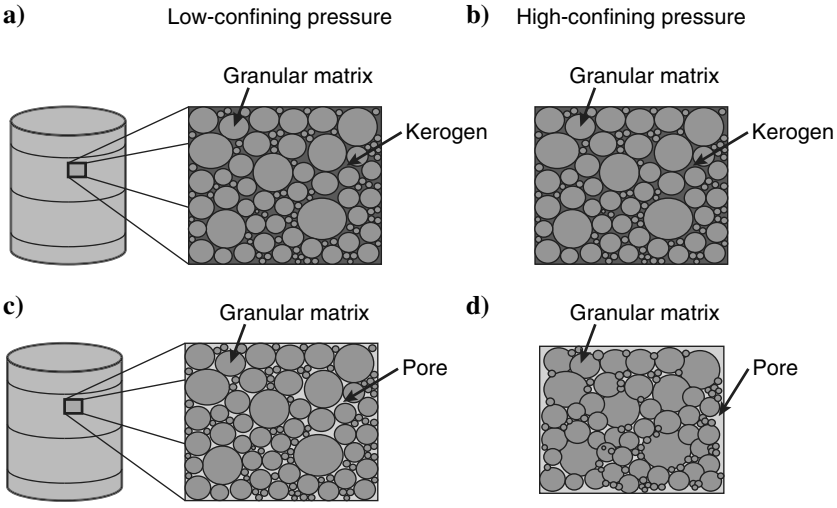

Figure 24. The conceptual model for micrite or siltstone evolution upon thermal maturation as a function of confining pressure. Four stages of evolution are shown: (a) immature sample at low confining pressure, (b) immature sample at high confining pressure, (c) gas window sample at low confining pressure, and (d) gas window sample at high confining pressure.

velocities, but not predictable changes in elastic anisotropy as we see for laminar shales. The loss of load-bearing, pore-filling material means that postfluid migration, in the absence of severe re-compaction, the acoustic signature of increased thermal maturity will be preserved.

Additionally, this conceptual model is applicable to the nonlaminar Woodford sample presented in Allan et al. (2014). The more directionally independent, isotropic evolution of the elastic properties of the weakly aligned Green River sample is a direct reflection of the behavior exhibited by the Woodford sample. The Woodford sample was also best described as a clay-poor siltstone rather than a "classic" shale, and, subsequently, we determine that our conceptual model for the thermal evolution of the Green River will be applicable to any nonlaminar shale or organic-rich micrite or siltstone.

Finally, it is important that we consider the pressures acting on the evolving organic-rich samples. The applied experimental confining pressures during the velocity and pyrolysis experiments are hydrostatic. In situ, the confining pressures will commonly deviate from hydrostatic. Subsequently, the textural and mechanical evolution observed in this study may be different from the natural evolution that would occur in nonhydrostatic regimes. Future work can address whether such a pressure dependence exists by performing velocity and pyrolysis experiments under different pressure regimes, e.g., triaxial pressures.

CONCLUSION

We have documented a set of pioneering experiments that characterize the elastic properties and microstructure of organic-rich shale after pyrolysis under representative reservoir confining pressures. By conducting these experiments on two end-member mudstones — one a clay-rich laminar shale, the other an argillaceous dolomicrite — we are able to present evolutionary trends that should encompass a broad range of intermediary shales. Pyrolysis-induced thermal maturation of the laminar Barnett Shale leads to the formation of submicrometer-scale cracks that preferentially align subparallel to bedding, most likely as a result of hydrocarbon generation. The development of this compliant porosity results in an up to 13% decrease in acoustic velocity perpendicular to bedding at low-confining pressures. However, at confining pressures greater than 20 MPa and in the absence of pore fluid pressure, the cracks close and the shale becomes acoustically indistinguishable from the prepyrolysis rock. Contrastingly, there are no observed aligned features formed as a result of induced thermal maturation of the weakly aligned Green River sample. Rather, the Green River samples exhibit a consistent, more isotropic decrease in acoustic velocities (up to 20%) as load-bearing, pore-filling kerogen is removed from the interlocking crystalline microstructure. The measured anisotropic increase in the Green River sample does not exhibit the pressure sensitivity expected for aligned microcracks, further evidence of the lack of aligned compliant feature development in the micritic sample.

In situ, so long as induced, aligned cracks remain open, laminar shales that have experienced thermal maturation, and subsequently may still contain hydrocarbons, may be identifiable by an increase in elastic anisotropy. Conversely, fluid expulsion or migration-induced closure of the cracks will reduce, or potentially remove entirely, the anisotropic signature of thermal maturation. In organic-rich nonlaminar shales, micritic rocks, or siltstones, in which kerogen occurs as an unstructured, load-bearing, pore-filling phase, regions of thermal maturation will be identifiable at high frequencies by decreases in the velocity of the layer; however, we do not expect a significant or predictable anisotropic signature to be developed due to the absence of aligned, compliant features.

Subsequently, the demonstration of anisotropic evolution as a function of thermal maturity may be used to better inform microseismic inversions, where well-log coverage enables the prediction of elastic anisotropy. The existence of an anisotropic signature in laminar shales should enable the identification of more mature, higher hydrocarbon potential horizons when implemented with organic richness estimates. The complex anisotropic response of nonlaminar, micritic rocks, however, may prevent the implementation of such an analysis in weakly aligned horizons.

ACKNOWLEDGMENTS

This work was sponsored by ENI S.p.A. under the Leland Stanford Junior University-ENI S.p.A. Umbrella Research Agreement. We thank ENI S.p.A. and Chevron for providing the samples used in this study. The authors thank L.-M. Joubert for her assistance with SEM imaging and S. Graham and A. Carroll for their detailed comments on the Green River sample. We acknowledge access to the beamline 11-ID-C at the APS of Argonne National Laboratory for texture measurements and help by Y. Ren. The authors also acknowledge the Stanford Rock Physics and Borehole Geophysics Project and Stanford University School of Earth Sciences for their support. A. M. Allan is funded by The William R. and Sara Hart Kimball Stanford Graduate Fellowship Fund. H.-R. Wenk is

appreciative for support from NSF (EAR-1343908) and DOE (DE-FG02-05ER15637).

REFERENCES

Allan, A. M., W. Kanitpanyacharoen, and T. Vanorio, 2015, A multi-scale methodology for the analysis of velocity anisotropy in organic-rich shale: Geophysics, **80**, no. 4, C73–C88, doi: 10.1190/geo2014-0192.1.

Allan, A. M., T. Vanorio, and J. E. P. Dahl, 2014, Pyrolysis-induced P-wave velocity anisotropy in organic-rich shales: Geophysics, **79**, no. 2, D41–D53, doi: 10.1190/geo2013-0254.1.

Chesnokov, E., I. O. Bayuk, and M. Ammerman, 2010, Determination of shale stiffness tensor from standard logs: Geophysical Prospecting, **58**, 1063–1082, doi: 10.1111/j.1365-2478.2010.00864.x.

Dewhurst, D. N., and A. F. Siggins, 2006, Impact of fabric, microcracks and stress field on shale anisotropy: Geophysical Journal International, **165**, 135–148, doi: 10.1111/j.1365-246X.2006.02834.x.

Grechka, V., P. Singh, and I. Das, 2011, Estimation of effective anisotropy simultaneously with locations of microseismic events: Geophysics, **76**, no. 6, WC143–WC155, doi: 10.1190/geo2010-0409.1.

Hornby, B. E., 1998, Experimental laboratory determination of the dynamic elastic properties of wet, drained shales: Journal of Geophysical Research, **103**, 29945–29964, doi: 10.1029/97JB02380.

Johnston, J. E., and N. I. Christensen, 1995, Seismic anisotropy of shales: Journal of Geophysical Research, **100**, 5991–6003, doi: 10.1029/95JB00031.

Jones, L. E. A., and H. F. Wang, 1981, Ultrasonic velocities in Cretaceous shales from the Williston basin: Geophysics, **46**, 288–297, doi: 10.1190/1.1441199.

Kaarsberg, E. A., 1959, Introductory studies of natural and artificial argillaceous aggregates by sound-propagation and X-ray diffraction methods: Journal of Geology, **67**, 447–472, doi: 10.1086/626597.

Kobchenko, M., H. Panahi, F. Renard, D. K. Dysthe, A. Malthe-Sørenssen, A. Mazzini, J. Scheibert, B. Jamtveit, and P. N. Meakin, 2011, 4D imaging of fracturing in organic-rich shales during heating: Journal of Geophysical Research, **116**, B12201, doi: 10.1029/2011JB008565.

Kocks, U. F., C. Tomé, and H. R. Wenk, 2000, Texture and anisotropy: Preferred orientations in polycrystals and their effect on materials properties: Cambridge University Press.

Lewan, M. D., 1994, Assessing natural oil expulsion from source rocks by laboratory pyrolysis, *in* L. B. Magoon, and W. G. Dow, eds., The petroleum system — From source to trap: AAPG Memoir 60, 201–210.

Li, J., C. Li, S. A. Morton, T. Dohmen, K. Katahara, and M. N. Toksöz, 2014, Microseismic joint location and anisotropic velocity inversion for hydraulic fracturing in a tight Bakken reservoir: Geophysics, **79**, no. 5, C111–C122, doi: 10.1190/geo2013-0345.1.

MacBeth, C., 2004, A classification for the pressure-sensitivity properties of a sandstone rock frame: Geophysics, **69**, 497–510, doi: 10.1190/1.1707070.

Passey, Q. R., F. U. Moretti, and J. D. Stroud, 1990, A practical model for organic richness from porosity and resistivity logs: AAPG Bulletin, **74**, 1777–1794.

Pepper, A. S., and P. J. Corvi, 1995, Simple kinetic models of petroleum formation. Part I: Oil and gas generation from kerogen: Marine and Petroleum Geology, **12**, 291–319, doi: 10.1016/0264-8172(95)98381-E.

Peters, K. E., and M. R. Cassa, 1994, Applied source rock geochemistry, *in* L. B. Magoon, and W. G. Dow, eds., The petroleum system — From source to trap: AAPG Memoir 60, 93–120.

Sayers, C., L. den Boer, S. Dasgupta, and B. Goodway, 2015, Anisotropy estimate for the Horn River Basin from sonic logs in vertical and deviated wells: The Leading Edge, **34**, 296–306, doi: 10.1190/tle34030296.1.

Thomsen, L., 1986, Weak elastic anisotropy: Geophysics, **51**, 1954–1966, doi: 10.1190/1.1442051.

Vanorio, T., T. Mukerji, and G. Mavko, 2008, Emerging methodologies to characterize the rock physics properties of organic-rich shales: The Leading Edge, **27**, 780–787, doi: 10.1190/1.2944163.

Vasin, R., H.-R. Wenk, W. Kanitpanyacharoen, S. Matthies, and R. Wirth, 2013, Elastic anisotropy modeling of Kimmeridge shale: Journal of Geophysical Research, **118**, 3931–3956, doi: 10.1002/jgrb.50259.

Vernik, L., 1993, Microcrack-induced versus intrinsic elastic anisotropy in mature HC-source shales: Geophysics, **58**, 1703–1706, doi: 10.1190/1.1443385.

Vernik, L., and C. Landis, 1996, Elastic anisotropy of source rocks: Implications for hydrocarbon generation and primary migration: AAPG Bulletin, **80**, 531–544.

Vernik, L., and X. Liu, 1997, Velocity anisotropy in shales: A petrophysical study: Geophysics, **62**, 521–532, doi: 10.1190/1.1444162.

Vernik, L., and A. Nur, 1992, Ultrasonic velocity and anisotropy of hydrocarbon source rocks: Geophysics, **57**, 727–735, doi: 10.1190/1.1443286.

Wang, Z., 2002, Seismic anisotropy in sedimentary rocks, Part 2: Laboratory data: Geophysics, **67**, 1423–1440, doi: 10.1190/1.1512743.

Wenk, H. R., L. Lutterotti, P. Kaercher, W. Kanitpanyacharoen, L. Miyagi, and R. N. Vasin, 2014, Rietveld texture analysis from synchrotron diffraction images. II. Complex multiphase materials and diamond anvil cell experiments: Powder Diffraction, **29**, 220–232, doi: 10.1017/S0885715614000360.

Yenugu, M. R., 2014, Elastic, microstructural and geochemical characterization of kerogen maturity for shales: Ph.D. dissertation, University of Houston.

Zargari, S., M. Prasad, K. C. Mba, and E. D. Mattson, 2011, Organic maturity, hydrous pyrolysis and elastic property in shales: Canadian Unconventional Resources Conference, SPE 149403, doi: 10.2118/149403-MS.